nature physics

Article

https://doi.org/10.1038/s41567-024-02532-x

Geometry-driven migration efficiency of autonomous epithelial cell clusters

Received: 17 July 2022

Accepted: 6 May 2024

Published online: 19 June 2024

Check for updates

Eléonore Vercruysse[1,7], David B. Brückner[2,7] ✉, Manuel Gómez-González[3], Alexandre Remson[1], Marine Luciano[1], Yohalie Kalukula[1], Leone Rossetti[3], Xavier Trepat[3,4,5,6], Edouard Hannezo[2] ✉ & Sylvain Gabriele[1] ✉

The directed migration of epithelial cell collectives through coordinated movements plays a crucial role in various physiological processes and is increasingly understood at the level of large confluent monolayers. However, numerous processes rely on the migration of small groups of polarized epithelial clusters in complex environments, and their responses to external geometries remain poorly understood. To address this, we cultivate primary epithelial keratocyte tissues on adhesive microstripes to create autonomous epithelial clusters with well-defined geometries. We show that their migration efficiency is strongly influenced by the contact geometry and the orientation of cell–cell contacts with respect to the direction of migration. A combination of velocity and polarity alignment with contact regulation of locomotion in an active matter model captures quantitatively the experimental data. Furthermore, we predict that this combination of rules enables efficient navigation in complex geometries, which we confirm experimentally. Altogether, our findings provide a conceptual framework for extracting the interaction rules of active systems from their interaction with physical boundaries, as well as design principles for collective navigation in complex microenvironments.

Collective cell migration is a fundamental process in various physiological and pathological events, including wound healing[1], cancer metastasis[2] and morphogenesis[3]. Although extensive research has focused on the migration dynamics of large epithelial sheets both in vivo[4] and in vitro[5], numerous physiologically relevant scenarios involve small autonomous clusters navigating complex geometries and boundary conditions[6–8]. For instance, in vivo observations in *Drosophila* have highlighted the migration of small cell groups, ranging from a few cells in border cell migration to larger clusters of approximately 100 µm in the posterior lateral line primordium of zebrafish[4,9]. Similarly, highly polarized and persistent tumoral clusters of up to eight cells have been identified in patients with epithelial-originating cancers[2,10–12], emphasizing the importance of understanding cell cluster migration from a biophysical standpoint. Although previous in vitro studies have investigated aspects like cluster rotation[13], escape from confinement[14] and invasion into free areas[15–17], the comprehensive mechanisms governing the migration of autonomous epithelial clusters are still elusive, particularly in more complex geometric environments.

The migration of an epithelial cluster necessitates front–rear polarization, facilitated by axial and lateral intercellular adhesive interactions and cryptic lamellipodia[5,6,18–20]. Various interaction rules, including polarity alignment (PA), velocity alignment (VA),

[1]Mechanobiology & Biomaterials group, Research Institute for Biosciences, CIRMAP, University of Mons, Mons, Belgium. [2]Institute for Science and Technology Austria, Klosterneuburg, Austria. [3]Institute for Bioengineering of Catalonia (IBEC), The Barcelona Institute for Science and Technology (BIST), Barcelona, Spain. [4]Centro de Investigación Biomédica en Red en Bioingeniería, Biomateriales y Nanomedicina (CIBER-BBN), Barcelona, Spain. [5]Facultat de Medicina, Universitat de Barcelona, Barcelona, Spain. [6]Institució Catalana de Recerca i Estudis Avançats (ICREA), Barcelona, Spain. [7]These authors contributed equally: Eléonore Vercruysse, David B. Brückner. ✉e-mail: david.brueckner@ist.ac.at; edouard.hannezo@ist.ac.at; sylvain.gabriele@umons.ac.be

stress–polarity coupling (SPC) and contact regulation of locomotion (CRL)[21–25], have been proposed to elucidate collective migration in large epithelial monolayers[26]. However, distinguishing between these mechanisms and understanding their roles in guiding small epithelial clusters through complex geometrical environments pose notable challenges both theoretically and experimentally. Studying the behaviour of minimal cell clusters and their responses to well-defined geometrical boundaries could provide invaluable insights into the regulation of collective cell motion[19,27,28].

Cluster migration speed depends mainly on lateral adhesion

To tackle this, we conducted experiments using fish epidermal keratocytes derived directly from primary explant tissue, which offer a well-suited model for studying cell migration due to their rapid and persistent locomotion, simple and stable shape, and strong cell–cell interactions. We generated minimal cell clusters of various sizes and aspect ratios by culturing fish scales containing primary epithelial monolayers on flat substrates functionalized with adhesive microstripes of fibronectin (FN) of various widths[16] (Fig. 1a). A large monolayer of primary epithelial keratocytes proliferated from the explant and extended onto the adhesive micropatterns, eventually breaking down into autonomous epithelial clusters of various dimensions. By tracking the migration of these clusters, we observed a significant stretching of intercellular adhesive bonds, leading to local fragmentation within cell trains. The extension speed on a 15 µm microstripe (Extended Data Fig. 1a) upon fragmentation (Extended Data Fig. 1b,c) indicated an increase of the intercellular distance during the fingering process, demonstrating that cell–cell adhesive bonds are extensively stretched (up to two- to threefold), leading to local fragmentation in an autonomous cell train (Extended Data Fig. 1d).

Initially, by focusing on 15-µm-wide microstripes that allowed the formation of one-dimensional epithelial trains lacking lateral intercellular interactions (Fig. 1b), we exploited the natural variability of cell train lengths to investigate whether the migration speed of these minimal clusters was influenced by their length (Fig. 1c). The initial breakage from the monolayer into cell trains yielded trains of various lengths, with a rare break-up in later stages (Supplementary Videos 1 and 2). As reported for individual keratocytes[29], the cell trains were highly polarized and persistent (Supplementary Fig. 1, and Supplementary Videos 3 and 4). Interestingly, the cell trains were highly compact (Extended Data Fig. 2a), and their projected areas were constant over time, regardless of their length, demonstrating that they moved as a cohesive and single unit (Extended Data Fig. 2b). We found that keratocytes extended cryptic lamellipodia underneath the cell body of the preceding cell[30] (Extended Data Fig. 3 and Supplementary Videos 5). Such cryptic lamellipodia have been shown to be involved in polarization and cell sheet movement[31] and could explain the compact morphology of the cell trains. We then tracked the migration of cell trains of different lengths ($2 \leq L \leq 10$ cells) to determine whether their migration speed was modulated by the number of constituent cells L (Fig. 1d). Our findings revealed that the cell train migration speed ($2 \leq L \leq 10$) was like the speed of individual cells on 15-µm-wide microstripes[29] and independent of the number of constituent cells (Fig. 1e and Supplementary Fig. 2), even for longer cell trains with $11 \leq L \leq 18$ (Extended Data Fig. 4a). This suggests that intercellular axial contacts (defined as front to rear cell contacts in the direction of migration) did not influence global migration efficiency. This finding contradicts the classic view that cells farther from the leading edge and characterized by both axial and lateral contacts (Extended Data Fig. 4b–d) would behave less as migratory follower cells, as this would theoretically predict a decrease of global velocity with train length L (with a $1/L$ trend; Fig. 1f), instead suggesting a model where all cells are equally polarized (Fig. 1f).

To confirm these observations, we analysed the cell polarization using the mitochondrial potential membrane and Golgi complex localization as a readout of the cell polarization. Stationary and unpolarized keratocytes exhibited a rounded shape and a low MitoTracker (MT) intensity that increased immediately with their polarization (Fig. 1g, Extended Data Fig. 5a,b and Supplementary Video 6). All cells within migrating cell trains of any length showed a large MT signal (Fig. 1h), reflecting a high level of mitochondrial activity that was constant over time during the migration of individual cells (Extended Data Fig. 5c) and cell trains (Extended Data Fig. 5d,e and Supplementary Video 7). In addition, our results indicate that there is a linear correlation between MT intensity and cell train areas (Fig. 1h,i and Extended Data Fig. 5f). In contrast with individual keratocytes where microtubules are densely packed in the cell body and wrapped around the nucleus to form a cage[29,32], we found that microtubules in cell trains were mostly aligned with the axis of migration and started to extend cryptic lamellipodia (Extended Data Fig. 3), suggesting a polarized state[33]. In line with previous observations of polarized individual cells on narrow microstripes[34], the Golgi complex of individual cells in cell trains was positioned behind the nucleus and a few micrometres away from it (Extended Data Fig. 6), confirming cell polarization within a cell train. These findings indicate that cells within a train are metabolically active, polarized and contribute to the migration process to drive the length-independent collective motion.

Moving beyond one-dimensional cell trains, we examined larger epithelial clusters formed on microstripes of widths 30, 45 and 100 µm to investigate the role of lateral adhesive interactions in collective migration (Fig. 2a). Epithelial monolayers grew on FN microstripes and fragmented in epithelial clusters of controlled widths (Fig. 2b). These clusters were composed of compacted cells with cryptic lamellipodia (Extended Data Fig. 3), as observed in the primary epithelial monolayer. Time-lapse experiments indicated that these migrating epithelial clusters of various widths were highly persistent (Supplementary Videos 8 and 9). The constituent cells of these clusters exhibited directed motion along the main axis of the microstripes (Fig. 2c), suggesting that the relative cell position within a cluster was maintained during the whole migration process, regardless of the cluster width. Widening the cell cluster strongly decreased the migration velocity from 8.1 ± 3.9 µm min^{-1} ($n = 59$) for cell trains on 15-µm-wide microstripes to 3.3 ± 1.2 µm min^{-1} ($n = 51$) on 30-µm-wide microstripes, 2.5 ± 0.8 µm min^{-1} ($n = 118$) on 45-µm-wide microstripes and 2.2 ± 0.8 µm min^{-1} ($n = 64$) on 100-µm-wide microstripes (Fig. 2d). There was a slowly convergence towards the migration speed of large-scale epithelial monolayers (1.4 ± 0.4 µm min^{-1}; Extended Data Fig. 5f). This was unlikely to be due to neighbour-driven confinement, as we found similar cellular densities within the different epithelial cluster sizes (Fig. 2e).

To shed light on the role of the cell–cell adhesion, we induced chemical disruption of cell–cell junctions with triethylene glycol diamine tetraacetic acid (EGTA) (Extended Data Fig. 7a,b). After EGTA treatment, we observed a fragmentation of all epithelial clusters into individual cells. Interestingly, EGTA treatments performed on 30-µm-wide clusters and primary monolayers induced a speed-up of the cells, whereas the cell migration speed remained constant after EGTA treatment on single cells and 15-µm-wide clusters (Extended Data Fig. 7c). Altogether, we argue that these data show that the establishment of an increasing number of lateral, but not axial, contacts decreases the migration speed during collective migration.

Modelling the geometry-dependent cluster migration

The collective motion of confined cell clusters shows length-independent but width-dependent behaviour, indicating complex dynamics influenced by cell–cell interactions and cluster geometry. Despite theoretical proposals regarding various interaction types for collective migration[26], it is unclear which interactions are required to

https://doi.org/10.1038/s41567-024-02532-x

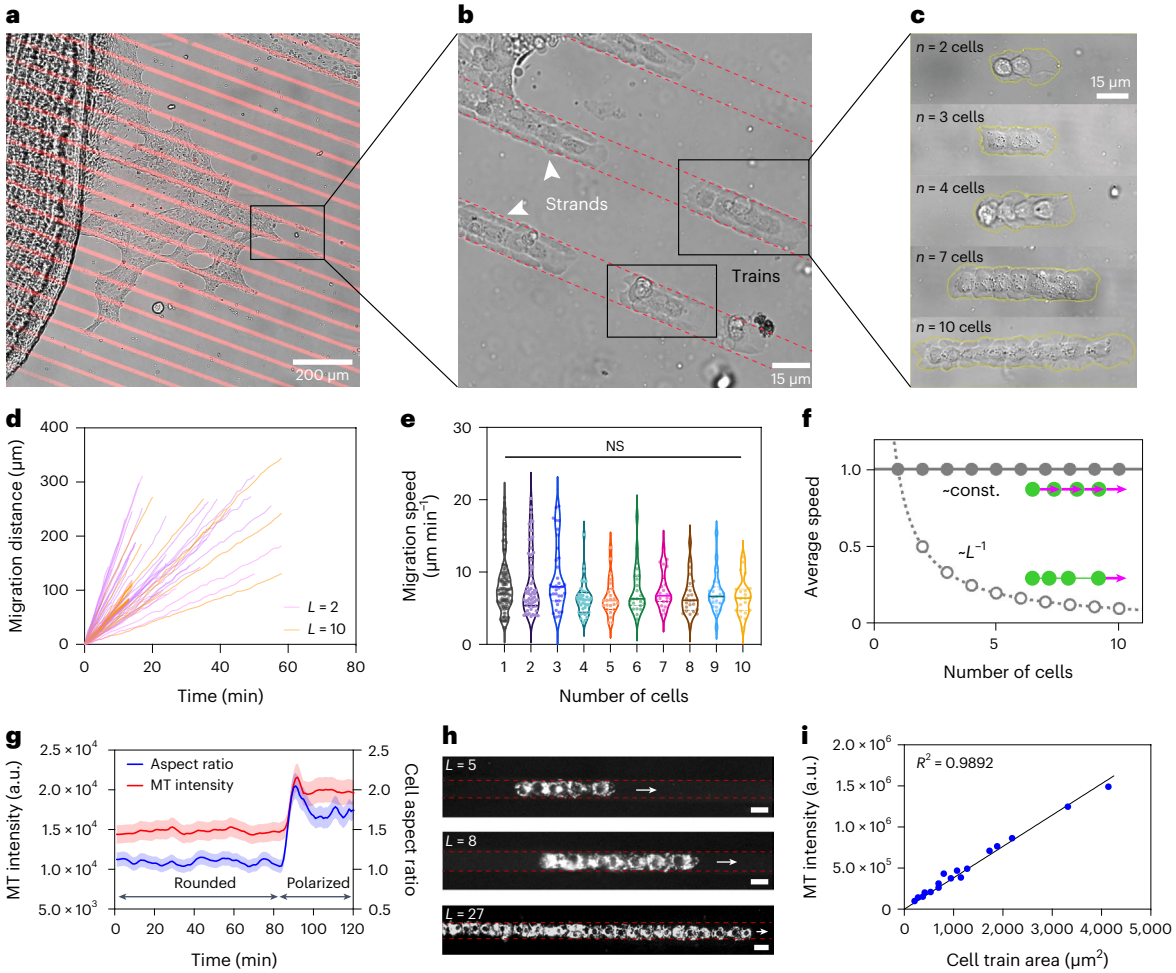

Fig. 1 | The migration velocity of cell trains is not affected by their length. **a**, A fish scale containing epithelial keratocytes on its internal side was deposited onto a PDMS substrate covered with FN microstripes 15 µm wide (red). **b**,**c**, The growth of the primary epithelial monolayer onto the FN microstripes leads to the formation of 'strands' (**b**) that break into randomly sized one-dimensional epithelial clusters called cell trains (**c**). **d**, Representative curves of the migration distance versus time for cell trains with $L = 2$ (purple) to $L = 10$ (orange). **e**, Migration speed of single cells with $L = 1$ ($n = 139$, black) and cell trains composed of different numbers of cells ($2 \le L \le 10$). Each point represents the mean migration speed of one cell train whose length (L) ranges from 2 to 10 cells, with $L = 2$ ($n = 65$, purple), $L = 3$ ($n = 35$, blue), $L = 4$ ($n = 39$, light green), $L = 5$ ($n = 23$, orange), $L = 6$ ($n = 24$, green), $L = 7$ ($n = 24$, pink), $L = 8$ ($n = 25$, brown), $L = 9$ ($n = 27$, light blue) and $L = 10$ ($n = 22$, yellow). A minimum of $N = 5$ replicates was used for each condition, and the total number of cell trains ($2 \le L \le 10$) was 284. **f**, Prediction of the speed as a function of the train length using a model of elastically coupled active particles with either all cells polarized (solid grey dots) or with only the leading cell polarized (open dots). const., constant. Purple arrows are vectors of polarization. **g**, Temporal evolution of MT intensity (red) and cell aspect ratio (blue) for individual keratocytes that underwent a polarization transition at $t = 88$ min and started to migrate. Data are means ± s.d. ($n = 6$ with $N = 3$ replicates). **h**, Live mitochondria stained with MT in cell trains of different lengths ($L = 5$, 8 and 27 cells). White arrows in show the direction of migration. Scale bars, 15 µm. **i**, The total MT intensity in cell trains is linearly proportional to their area, regardless of length. NS, not significant ($P = 0.8939 > 0.05$, Kruskal–Wallis test).

capture the migration dynamics of small confined epithelial clusters. To address this, we devised a minimal theoretical model of confined cell clusters. Considering our observations, we modelled cells as polar particles with positions $\mathbf{x}_i(t)$ at time t, which exert active migration forces in a direction of polarity $\mathbf{p}_i$ (defined in our system by the orientation of the lamellipodia), with each cell i connected to its neighbours j by elastic links (adhesion) modelled as linear elastic forces $\mathbf{F}^{\text{elastic}}$. This model is described by the non-dimensionalized equation $\mathrm{d}\mathbf{x}_i/\mathrm{d}t = \sum \mathbf{F}_j^{\text{elastic}} + \mathbf{p}_i(t)$. Importantly, this model allows cell velocities $\mathrm{d}\mathbf{x}_i/\mathrm{d}t$ and polarities $\mathbf{p}_i$ that are not necessarily equal to reflect cell–cell mechanical interactions. The evolution of the cell polarity was further modelled as $\mathrm{d}\mathbf{p}_i/\mathrm{d}t = \mathbf{F}^{\text{single}} + \mathbf{F}^{\text{int}} + \sqrt{2D}\boldsymbol{\eta}_i(t)$, where the single-cell term $\mathbf{F}^{\text{single}} = \mathbf{p}_i\left(1 - |\mathbf{p}_i|^2\right)$ describes the spontaneous polarization of single cells, and $\boldsymbol{\eta}_i(t)$ represents Gaussian white noise (see Supplementary Theory Note for details)[35].

The general interaction term $\mathbf{F}^{\text{int}}$ encompasses various cell–cell interactions that could underlie the intricate collective dynamics observed in confined cell clusters (Fig. 2f). Among these interactions, two classes have received particular attention: alignment and anti-alignment of neighbouring cells[22,26,36,37]. Indeed, our system demonstrates both alignment (Extended Data Fig. 8a) and anti-alignment (Extended Data Fig. 8b) in two-cell collision experiments, depending on the initial configuration[38]. Alignment phenomena are driven by the tendency of cells to flock in the same direction, which can be described by (1) alignment of the polarity of each individual cell to match its own VA[25,26] and (2) direct PA between neighbours[39,40]. On the other hand, a number of cell types have been shown to anti-align to counteract the forces exerted by their neighbours, either due to (1) SPC, in which cells exert polarity forces opposite to the stress applied on their cell–cell contacts[19,35,41], or (2) CRL, which controls cell polarity in response to cell–cell contacts[23]. Although CRL has been often studied in scenarios

https://doi.org/10.1038/s41567-024-02532-x

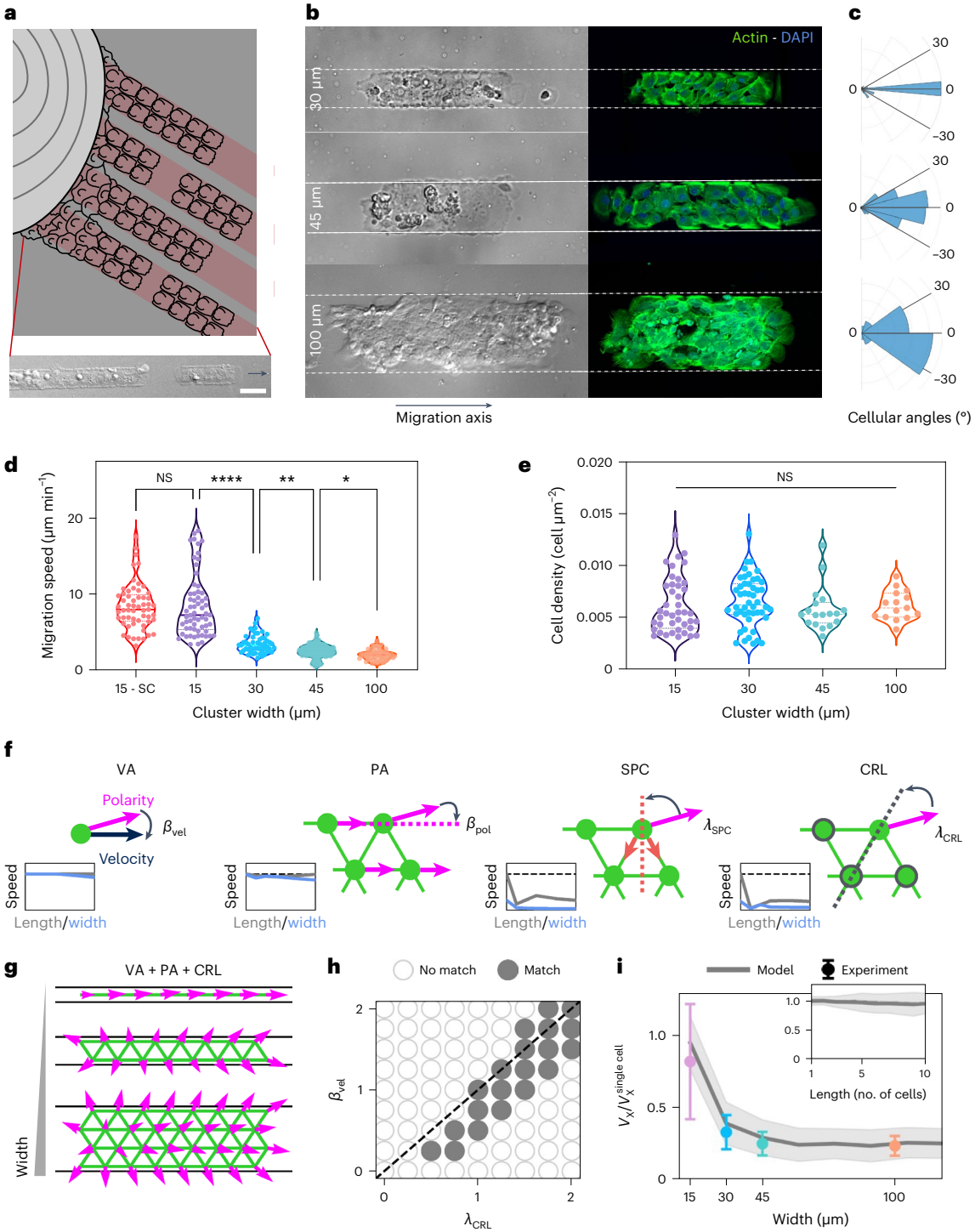

Fig. 2 | The migration velocity decreases as the epithelial cluster widens. **a**, Autonomous epithelial clusters form and detach from extensions of primary epithelial tissue growing on adhesive microstripes (light red). Inset, differential interference contrast (DIC) image of an epithelial cluster on a 30-µm-wide microstripe. Increasing the microstripe width gradually increased the cell–cell interactions. Grey arrow shows the direction of migration. Scale bar, 15 µm. **b**, DIC and epifluorescence image (actin in green and DAPI in blue) of epithelial clusters on FN microstripes of width 30, 45 or 100 µm. **c**, Distribution of migration angles within an epithelial cluster migrating for 60 min on 30 µm (top), 45 µm (middle) and 100 µm (bottom) wide microstripes. The horizontal axis is 0°. **d**,**e**, Distributions of migration speeds (**d**) and cell density (**e**) for single epithelial cells on 15-µm-wide microstripes (SC, pink) and clusters on 15-µm-wide (purple), 30-µm-wide (blue), 45-µm-wide (green) and 100-µm-wide (orange) microstripes, for $N \geq 5$ replicates for each condition. **f**, Sketch of VA, PA, SPC and CRL, quantified by amplitudes β_{vel}, β_{pol}, λ_{SPC} and λ_{CRL}, respectively (Supplementary Theory Note). Green dots and lines represent cells and elastic links between cells, respectively, while blue, magenta and red arrows denote the cell velocity, polarity and intercellular stress, respectively. Insets show predicted cluster speed dependence on length (grey) and width (light blue) for each mechanism. Dashed lines indicate the speed of a single cell. **g**, Predicted polarity fields as a function of cluster width for VA, PA and CRL combined. **h**, Phase diagram showing where VA + PA + CRL captures speed trends independent of length and decreasing with width (solid grey dots), as a function of the VA and CRL strength, with fixed $\beta_{pol} = 1.5$. Similar trends were observed for other β_{pol} (Supplementary Theory Note). Black dashed line indicates equal values of β_{vel} and λ_{CRL}. **i**, Predicted speed dependence on width and length with best-fitting parameters $\beta_{vel} = 0.15$, $\beta_{pol} = 1.5$ and $\lambda_{CRL} = 0.5$, compared to experimental data, both normalized by the single-cell speed. Error bars denote standard deviations. Shaded areas indicate standard error of the mean (s.e.m.). $^{*}P < 0.05$, $^{**}P < 0.01$, $^{****}P < 0.0001$ (post hoc Dunn's test), with $P < 0.0001$ for **d** and $P > 0.05$ for **e** using Kruskal–Wallis tests.

https://doi.org/10.1038/s41567-024-02532-x

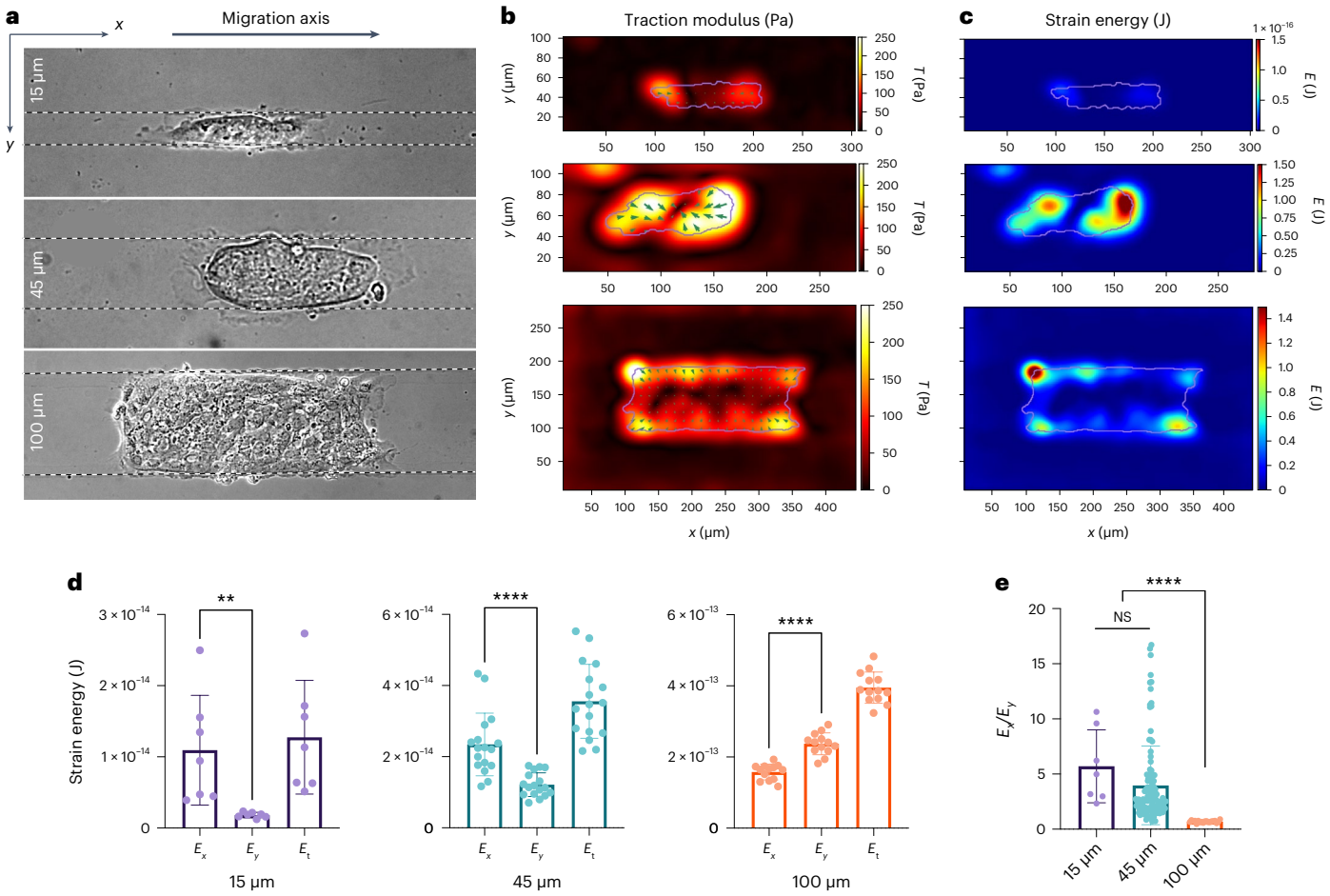

Fig. 3 | Widening epithelial clusters leads to the emergence of lateral contractile forces and lateral intracellular stresses. a, Typical DIC images of epithelial clusters on 15-, 45- and 100-µm-wide microstripes. **b**,**c**, Heat maps of the spatial distributions of the traction modulus (**b**) and of the strain energy field exerted on the substrate (**c**) during the migration of epithelial clusters 15, 45 or 100 µm wide. **d**,**e**, Distribution of the axial (E_x) and lateral (E_y) components of the total strain energy (E_t) (**d**) and ratio E_x/E_y (**e**) for epithelial clusters 15 µm wide (purple), 45 µm wide (green) and 100 µm wide (orange). $^{**}P < 0.01$, $^{****}P < 0.0001$. Error bars denote standard deviations.

involving two isolated cells colliding and repolarizing[42], we consider it here in the broader context of strong adhesion between cells, which is important in a number of physiologically relevant situations[42,43]. Our minimal model accounts for all possible couplings allowed by symmetry and aligns with these categories (Supplementary Theory Note). This raises a crucial question. Could several distinct interaction types interact to produce the observed non-trivial coupling to cluster geometry?

We proceeded to simulate clusters with various lengths and widths and considered each possible combination of interaction types. Alignment interactions (PA or VA) typically result in a geometry-independent speed, with all cells moving together in a specific direction, whereas anti-alignment interactions (SPC or CRL) lead to a rapid decrease in speed with increasing length and width, as clusters tend to develop a bidirectional polarity pattern (Fig. 2g and Supplementary Video 6). However, we hypothesized that combining different mechanisms to achieve alignment in the axial direction and anti-alignment in the lateral direction might explain our data. Our model revealed that pairwise combinations of interactions could still not qualitatively capture our observations (Supplementary Theory Note and Supplementary Video 10). However, we found that the combination of VA, PA and CRL represents the minimal interactions necessary to reproduce length-independent but width-dependent migration (Fig. 2h). Qualitatively, this combination of interactions causes length-independent aligned cell motion in the axial direction, whereas the presence of boundaries along the lateral direction renders such an aligned state impossible, allowing lateral anti-alignment to develop as it is driven by the tendency from CRL in which boundary cells polarize outwards (Fig. 2g). Here, VA and PA play distinct roles. VA breaks the symmetry the between axial and lateral directions, preventing non-zero global velocities in the lateral direction, whereas PA propagates the CRL-driven outward-pointing polarity into the bulk, causing a reorientation of the polarity that hinders productive motion, which can occur only in the axial direction. When the VA and CRL magnitudes are similar, this interplay of geometry and interactions results in the observed trends of speed being independent of length but decreasing with width (Fig. 2h,i and Supplementary Video 11).

Furthermore, we explored different model extensions to investigate the effects of adhesion strength and cell-to-cell variability on prediction robustness. We checked that the constant cell speed of cellular trains was not an artefact due to cells with different intrinsic speeds detaching from each other by including the possibility of junctional breakage (when the cell–cell distance exceeds a critical threshold l_c; Supplementary Theory Note and Supplementary Fig. 5), as well as intrinsic variability in cellular migration forces (based on single-cell migration speed variability; Supplementary Theory Note and Supplementary Fig. 5). For low adhesion, trains frequently broke apart, even due to intrinsic variability and noise on protrusion forces,

https://doi.org/10.1038/s41567-024-02532-x

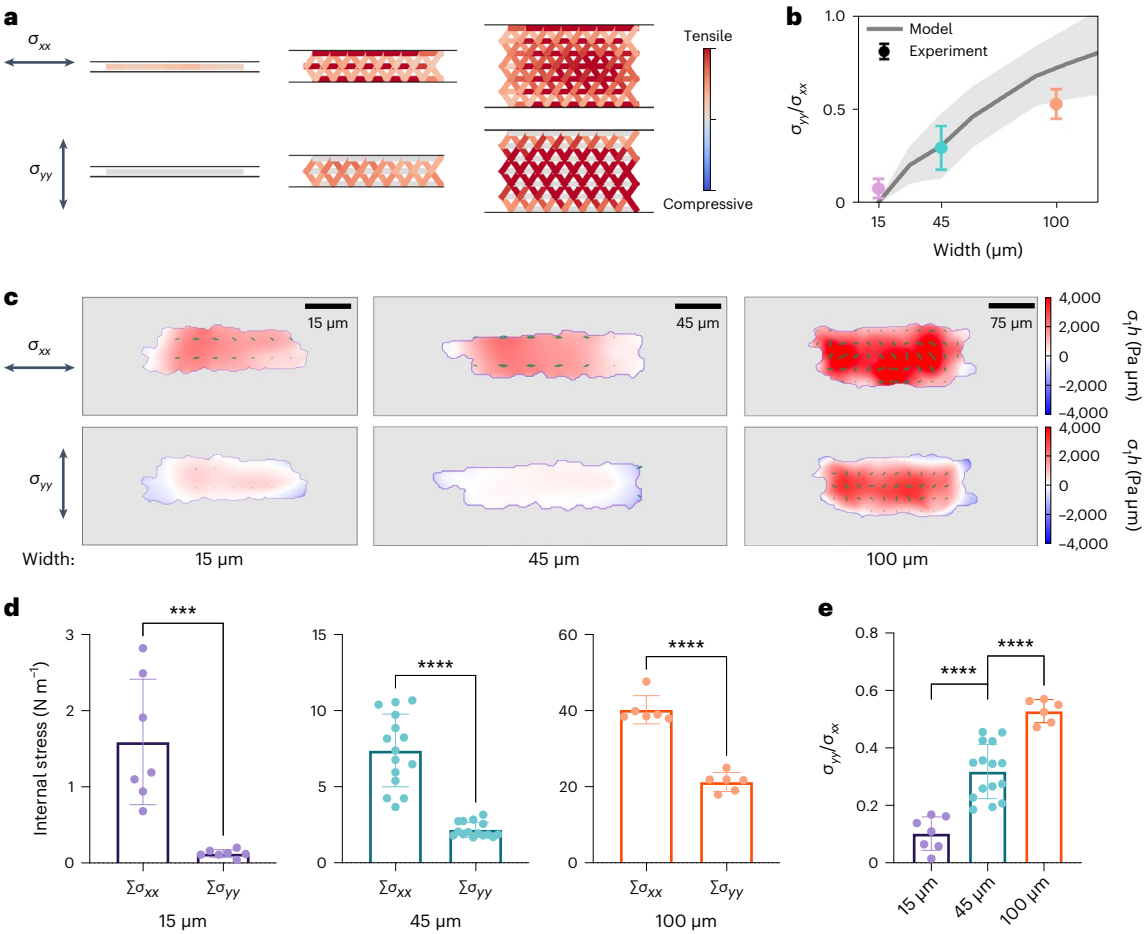

Fig. 4 | The lateral internal stress increases in wider epithelial clusters. **a**, Theoretical predictions of axial (σ_{xx}; top) and lateral (σ_{yy}; bottom) components of the internal stress field for various cluster widths (one, three and seven cells, corresponding to widths of 15, 45 or 100 μm) using the VA + PA + CRL model. **b**, Ratio of the lateral to axial stress σ_{yy}/σ_{xx} as a function of cluster width as predicted by the model with best parameters identified based on cell speed (Fig. 2i). Shaded area indicates standard error of the mean (s.e.m.). **c**, Typical maps of the spatial distribution of the axial (σ_{xx}) and lateral (σ_{yy}) internal stress components for cell trains 15 μm wide (light purple) and epithelial clusters 45 μm wide (light green) or 100 μm wide (light orange). **d**,**e**, Quantification of σ_{xx} and σ_{yy} (**d**) and ratio σ_{yy}/σ_{xx} (**e**). ***$P < 0.001$, ****$P < 0.0001$. Error bars denote standard deviations.

in sharp contrast to our observations of extremely rare detachments, in both trains and confluent tissues. These analyses allowed us to estimate a lower bound for the adhesion force in fish keratocytes (Supplementary Theory Note). An upper bound of the adhesion forces can also be obtained from explicit modelling of the initial fingering process in which trains detach from the bulk due to the very high cellular stretches arising from the microstripe constraint (Extended Data Fig. 1, Supplementary Video 12 and Supplementary Theory Note).

Together, these findings demonstrate how several types of cell–cell interactions interplay to determine the geometry-dependent migration efficiency of cell clusters, which emphasizes the role of strong cell–cell adhesion in maintaining cluster cohesion even in the presence of outward-pointing polarities.

Experimental test of the predicted interaction regime

Our model yields a clear and experimentally verifiable prediction: the outward polarization induced by CRL at the boundary, propagated by PA, leads to a build-up of lateral intercellular stress, which we anticipate will increase with cluster width. To test this, we conducted traction force microscopy experiments to quantify the orientation of the traction forces generated by cell clusters of various geometries. To discern the axial component (along the microstripe axis) and the lateral component (perpendicular to the microstripe axis) of the traction stresses (Fig. 3a), we represented tractions in a reference frame where the horizontal and vertical axes (x, y) corresponded to the length and width of the cell cluster, respectively. As shown in Fig. 3b, cell trains exhibited a force dipole concentrated at both ends of the cell train, directed inward towards the centre, which indicates that there was robust intercellular coupling[5]. Intriguingly, widening cell clusters to 45 or 100 μm resulted in more prominent lateral traction forces. By computing the strain energy as the dot product of the traction force with displacement (Fig. 3c), we assessed the individual contribution of the axial (E_x) and lateral (E_y) components of the strain energy. In agreement with the force dipole, cell trains on a 15-μm-wide microstripe displayed a substantial axial component, constituting approximately 96.7% of the total strain energy (Fig. 3d), whereas the lateral component was negligible (approximately 4.3%). Notably, the lateral component E_y increased with width, even causing a reversal of the major strain energy component for 100-μm-wide clusters, with E_y accounting for approximately 27.1% and 56.4% of the total strain energy for 45- and 100-μm-wide clusters, respectively (Fig. 3d). As shown in Fig. 3e, widening cell clusters thus leads to the inversion of the major strain energy component for 100-μm-wide clusters. Collectively, these findings indicate that there was a transition between axial and lateral contractile forces that is dependent on cluster width, such that the augmented traction forces in wider cell clusters are exerted normal to the migration direction.

https://doi.org/10.1038/s41567-024-02532-x

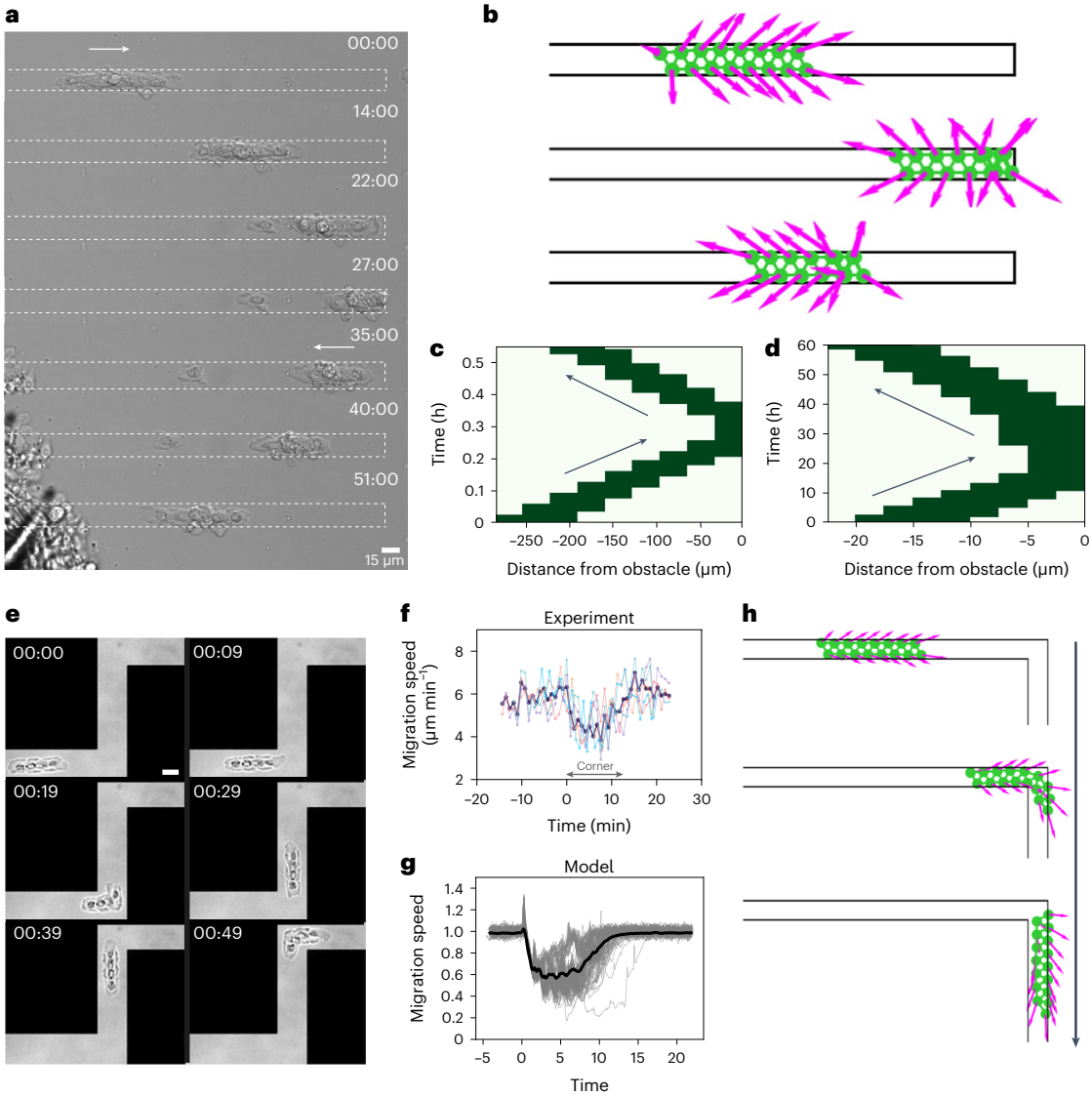

Fig. 5 | Navigation of cell trains in dead ends and complex microenvironments. a, Time-lapse sequence of the migration of a one-dimensional cluster moving towards the border of a 15-µm-wide FN microstripe (from left to right) over 51 min. After reaching the micropattern extremity on the left part, the cell train compacted against the border; then the epithelial cells repolarized and the cluster migrated in the opposite direction (from right to left). White arrows show the direction of migration. **b**, Simulation of the migration of a one-dimensional epithelial cluster migrating from the left to the right towards an obstacle. The combination of VA + PA + CRL allows the cell train to repolarize towards the opposite direction after the collision. **c**, Kymograph of the spatial position over time of the cell train presented in **a**, showing its repolarization after the collision. The slopes before and after the collision indicate the similar migration velocities. **d**, Kymograph of the spatial position over time of the simulated cell train in **b**, showing its fast repolarization after the collision and absence of stalling at the boundary. The slopes before and after the collision indicate the similar migrating velocities. **e**, Time-lapse sequence in DIC mode of a cell train migrating on a microstripe 15 µm wide with corners of 90°. The duration was 49 min. Scale bar is 15 µm. **f**, Superimposed representation of the migration speed of cell trains ($L = 4$ cells and $n = 5$ from three replicates) around corners of 90°. The bold curve in purple represents the mean velocity. **g**, Predicted speed evolution around a corner of 90°, showing a similar decrease as in the experiment and the subsequent recovery of the initial speed. Thin grey curves correspond to simulations of 100 individual clusters. The black curve represents the average behaviour. **h**, Time-series of simulated cell clusters navigating around corners of 90°, showing efficient repolarization.

Given that traction forces must be counterbalanced by internal forces transmitted within and between cells, we can infer the spatio-temporal profile of the stress tensor within the monolayer using monolayer stress microscopy (MSM), which we used to calculate the axial (σ_{xx}) and lateral (σ_{yy}) components of the internal stress field[44]. Our model predicted a minimal amount of lateral stress in cell trains 15 µm wide, which increased as the cluster widened (Fig. 4a). Notably, we demonstrated through confocal microscopy that keratocytes extend cryptic lamellipodia against the substratum beneath the cells in front of them (Extended Data Fig. 3). More quantitatively, our model (with parameters fully constrained based solely on the speed variations as a function of cluster geometry; Fig. 2i) quantitatively predicted the increase in the stress ratio σ_{yy}/σ_{xx} with cluster width (Fig. 4b), and the results are aligned with MSM experiments conducted on 15-, 45- and 100-µm-wide clusters (Fig. 4c). The agreement between our theoretical results (Fig. 4b) and the experimental results (Fig. 4e) underscores the significance of the lateral stress component in wide epithelial clusters, as well as the cooperative role of several modes of cell–cell interaction in shaping the collective migration and stress profile of small cell clusters.

Migration efficiency in response to complex boundaries

The cell polarization fields predicted by our model suggest that there are non-trivial consequences for the lamellipodial orientation, which reflects the competing effects of axial and lateral cell–cell interactions. These effects are particularly evident at lateral boundaries. To assess the lateral components attributed to CRL, we imaged cell clusters reaching the end of a microstripe that leads to an open space (Extended Data Fig. 9a and Supplementary Video 13). These clusters promptly developed large lamellipodia in the lateral direction away from their neighbours, consistent with the assumption of CRL in the model and validated by simulations for this scenario (Extended Data Fig. 9b and Supplementary Video 14). Crucially, even in this scenario, the cell trains remained intact, supporting our assumption of the robust adhesion that mediates the mechanical and polarity interactions between cells (Extended Data Fig. 10 and Supplementary Theory Note).

The combination of interaction mechanisms with opposing effects, which cause substantial unproductive lateral stresses and slow the collective migration, prompted an inquiry into their functional implications. Using our model, we predicted how different cell–cell interaction combinations determined cluster behaviour in complex external environments. In geometries featuring blind ends requiring sudden polarization changes, the selection of cell–cell interactions strongly influences the repolarization behaviour (Fig. 5a–d, Extended Data Fig. 10a–f and Supplementary Video 15). Although the VA and PA mechanisms facilitated rapid migration along uninterrupted straight microstripes, they exhibited poor repolarization capabilities. Conversely, CRL, although it led to slow-moving clusters, enabled swift repolarization upon alterations in contact geometry. The parameter space reflecting intermediate values of all three interaction parameters, consistent with experimental observations, demonstrated seemingly optimal behaviour with both rapid straight migration and obstacle-driven repolarization (Extended Data Fig. 10b). Time-lapse experiments and quantitative cell tracking of epithelial clusters reaching the end of a FN stripe corroborated the theoretical prediction, with fast and global repolarization of both cell trains and clusters (Extended Data Fig. 10d–f).

To assess the generalizability of these findings, we further challenged cell cluster migration with geometries featuring 120° corners (Extended Data Fig. 10g) and 90° angles (Fig. 5e and Supplementary Video 16). Our experimental results reveal that the cell clusters efficiently navigated these intricate boundary conditions. They remained cohesive without fragmentation despite the induced velocity orientation gradients. The evolution of the migration speed around the sharpest angle corners showed that cell trains experienced only a partial and transient speed reduction while circumventing an obstacle (Extended Data Fig. 10h). Aggregating several experiments on cell trains of $L = 5$ cells revealed an approximately 30% speed decrease (Fig. 5f). These observations were captured by our model, which forecast that cell clusters would retain their cohesiveness and rapidly reorient. Specifically, the model predicted a speed decrease like that observed experimentally, with cell trains returning to their initial speed after a brief period (Fig. 5g), thus demonstrating efficient repolarization (Fig. 5h and Supplementary Video 17). Together, these findings not only corroborate the validity of the VA + PA + CRL combination but also suggest a potential functional significance of these specific interactions in enabling cell clusters to navigate complex microenvironments.

Our findings contrast with observations of other cell types for which flocking behaviour was evident under periodic boundary conditions[19]. We observed that trains of Madin–Darby canine kidney (MDCK) cells failed to achieve coherent polarization under open boundary conditions, consistent with theoretical predictions (Supplementary Fig. 4). This behaviour was predicted by reducing the amplitude of the VA, resulting in a frustrated state with outward polarization for cell trains on microstripes and coherent migration with collective polarization in a periodic system (Supplementary Video 18). Furthermore, our model (VA + PA + CRL) successfully recapitulates the behaviour of keratocytes and MDCK cells (Supplementary Video 19), highlighting the broader implications of boundary conditions in shaping cell cluster dynamics.

Online content

Any methods, additional references, Nature Portfolio reporting summaries, source data, extended data, supplementary information, acknowledgements, peer review information; details of author contributions and competing interests; and statements of data and code availability are available at https://doi.org/10.1038/s41567-024-02532-x.

References

1. Lauffenburger, D. A. & Horwitz, A. F. Cell migration: a physically integrated molecular process. *Cell* **84**, 359–369 (1996).
2. Friedl, P. et al. Migration of coordinated cell clusters in mesenchymal and epithelial cancer explants in vitro. *Cancer Res.* **55**, 4557–4560 (1995).
3. Friedl, P. & Gilmour, D. Collective cell migration in morphogenesis, regeneration and cancer. *Nat. Rev. Mol. Cell Biol.* **10**, 445–457 (2009).
4. Weijer, C. J. Collective cell migration in development. *J. Cell Biol.* **122**, 3215–3223 (2009).
5. Serra-Picamal, X. et al. Mechanical waves during tissue expansion. *Nat. Phys.* **8**, 628–634 (2012).
6. Gopinathan, A. & Gov, N. S. Cell cluster migration: connecting experiments with physical models. *Semin. Cell Dev. Biol.* **93**, 77–86 (2019).
7. Dai, W. et al. Tissue topography steers migrating *Drosophila* border cells. *Science* **370**, 987–990 (2020).
8. Marchant, C. L., Malmi-Kakkada, A. N., Espina, J. A. & Barriga, E. H. Cell clusters softening triggers collective cell migration in vivo. *Nat. Mater.* **21**, 1314–1323 (2022).
9. Bianco, A. et al. Two distinct modes of guidance signalling during collective migration of border cells. *Nature* **448**, 362–365 (2007).
10. Hou, J.-M. et al. Circulating tumor cells as a window on metastasis biology in lung cancer. *Am. J. Pathol.* **178**, 989–996 (2011).
11. Carlsson, A. et al. Circulating tumor microemboli diagnostics for patients with non–small-cell lung cancer. *J. Thorac. Oncol.* **9**, 1111–1119 (2014).
12. Cheung, K. J. & Ewald, A. J. A collective route to metastasis: seeding by tumor cell clusters. *Science* **352**, 167–169 (2016).
13. Segerer, F. J., Thüroff, F., Piera Alberola, A., Frey, E. & Rädler, J. O. Emergence and persistence of collective cell migration on small circular micropatterns. *Phys. Rev. Lett.* **114**, 228102 (2015).
14. d'Alessandro, J. et al. Contact enhancement of locomotion in spreading cell colonies. *Nat. Phys.* **13**, 999–1005 (2017).
15. Peyret, G. et al. Sustained oscillations of epithelial cell sheets. *Biophys. J.* **117**, 464–478 (2019).
16. Vedula, S. R. K. et al. Emerging modes of collective cell migration induced by geometrical constraints. *Proc. Natl Acad. Sci. USA* **109**, 12974–12979 (2012).
17. Pagès, D.-L. et al. Cell clusters adopt a collective amoeboid mode of migration in confined nonadhesive environments. *Sci. Adv.* **8**, eabp8416 (2022).
18. Hayer, A. et al. Engulfed cadherin fingers are polarized junctional structures between collectively migrating endothelial cells. *Nat. Cell Biol.* **18**, 1311–1323 (2016).
19. Jain, S. et al. The role of single-cell mechanical behaviour and polarity in driving collective cell migration. *Nat. Phys.* **16**, 802–809 (2020).
20. Luciano, M. et al. Appreciating the role of cell shape changes in the mechanobiology of epithelial tissues. *Biophys. Rev.* **3**, 011305 (2022).
21. Alert, R. & Trepat, X. Living cells on the move. *Phys. Today* **74**, 30–36 (2021).

22. Brückner, D. B. et al. Learning the dynamics of cell–cell interactions in confined cell migration. *Proc. Natl Acad. Sci. USA* **118**, e2016602118 (2021).
23. Zisis, T. et al. Disentangling cadherin-mediated cell–cell interactions in collective cancer cell migration. *Biophys. J.* **121**, 44–60 (2022).
24. Copenhagen, K. et al. Frustration-induced phases in migrating cell clusters. *Sci. Adv.* **4**, eaar8483 (2018).
25. Basan, M., Elgeti, J., Hannezo, E., Rappel, W.-J. & Levine, H. Alignment of cellular motility forces with tissue flow as a mechanism for efficient wound healing. *Proc. Natl Acad. Sci. USA* **110**, 2452–2459 (2013).
26. Alert, R. & Trepat, X. Physical models of collective cell migration. *Annu. Rev. Condens. Matter Phys.* **11**, 77–101 (2020).
27. Duclos, G. et al. Spontaneous shear flow in confined cellular nematics. *Nat. Phys.* **14**, 728–732 (2018).
28. George, M., Bullo, F. & Campàs, O. Connecting individual to collective cell migration. *Sci. Rep.* **7**, 9720 (2017).
29. Mohammed, D. et al. Substrate area confinement is a key determinant of cell velocity in collective migration. *Nat. Phys.* **15**, 858–866 (2019).
30. Ozawa, M. et al. Adherens junction regulates cryptic lamellipodia formation for epithelial cell migration. *J. Cell Biol.* **219**, e202006196 (2020).
31. Farooqui, R. & Fenteany, G. Multiple rows of cells behind an epithelial wound edge extend cryptic lamellipodia to collectively drive cell-sheet movement. *J. Cell Sci.* **118**, 51–63 (2005).
32. Kalukula, Y., Stephens, A. D., Lammerding, J. & Gabriele, S. Mechanics and functional consequences of nuclear deformations. *Nat. Rev. Mol. Cell Biol.* **23**, 583–602 (2022).
33. Etienne-Manneville, S. Microtubules in cell migration. *Annu. Rev. Cell Dev. Biol.* **29**, 471–499 (2013).
34. Pouthas, F. et al. In migrating cells, the Golgi complex and the position of the centrosome depend on geometrical constraints of the substratum. *J. Cell Sci.* **121**, 2406–2414 (2008).
35. Banerjee, S., Utuje, K. J. C. & Marchetti, M. C. Propagating stress waves during epithelial expansion. *Phys. Rev. Lett.* **114**, 228101 (2015).
36. Barton, D. L., Henkes, S., Weijer, C. J. & Sknepnek, R. Active vertex model for cell-resolution description of epithelial tissue mechanics. *PLoS Comput. Biol.* **13**, e1005569 (2017).
37. Bertrand, T. et al. Clustering and ordering in cell assemblies with generic asymmetric aligning interactions. *Phys. Rev. Res.* **6**, 023022 (2024).
38. Li, D. & Wang, Y. Coordination of cell migration mediated by site-dependent cell–cell contact. *Proc. Natl Acad. Sci. USA* **115**, 10678–10683 (2018).
39. Vicsek, T., Czirók, A., Ben-Jacob, E., Cohen, I. & Shochet, O. Novel type of phase transition in a system of self-driven particles. *Phys. Rev. Lett.* **75**, 1226–1229 (1995).
40. Debets, V. E., Janssen, L. M. C. & Storm, C. Enhanced persistence and collective migration in cooperatively aligning cell clusters. *Biophys. J.* **120**, 1483–1497 (2021).
41. Weber, G. F., Bjerke, M. A. & DeSimone, D. W. A mechanoresponsive cadherin-keratin complex directs polarized protrusive behavior and collective cell migration. *Dev. Cell* **22**, 104–115 (2012).
42. Stramer, B. & Mayor, R. Mechanisms and in vivo functions of contact inhibition of locomotion. *Nat. Rev. Mol. Cell Biol.* **18**, 43–55 (2017).
43. Trepat, X. et al. Physical forces during collective cell migration. *Nat. Phys.* **5**, 426–430 (2009).
44. Tambe, D. T. et al. Monolayer stress microscopy: limitations, artifacts, and accuracy of recovered intercellular stresses. *PLoS ONE* **8**, e55172 (2013).

Methods

PDMS-coated glass coverslips

Glass coverslips (170 µm thick) coated with polydimethylsiloxane (PDMS) were fabricated by spin-coating[45], as previously described[46]. Briefly, PDMS was prepared from a commercially available silicone elastomer kit (Sylgard 184, Dow Corning) by mixing the curing agent and the base (1:10 ratio) thoroughly for 2 min. The mixture was degassed and spin-coated at 5,000 rpm on clean 25 mm glass coverslips to obtain a thin PDMS layer ~30 µm thick. The PDMS layer was then cured for 3 h at 60 °C, flushed with ethanol and exposed to ultraviolet illumination for 15 min. The PDMS-coated glass coverslips were then stored in the dark at room temperature in a Petri dish until use.

Microcontact printing

PDMS stamps were used to create an FN micropattern on the PDMS-coated glass coverslips. A PDMS mixture (Sylgard 184, Dow Corning) was obtained by mixing the curing agent and the base (1:10 ratio) thoroughly for 2 min. After degassing, the mixture was poured onto a microstructured silicon wafer, which had previously been functionalized with fluorosilane vapour (tridecafluoro-1,1,2,2-tetrahydrooctyl-1-trichlorosilane, Gelest) under vacuum to facilitate the removal of the PDMS layer (~1 cm thick)[47]. After curing overnight at 65 °C, the PDMS block was peeled off and cut into stamps of approximately 1 cm^2. The PDMS stamps were washed in an ultrasonic bath with detergent solution (Decon 90, 5%) for 30 min at 35 °C, then with isopropanol (70%) for 15 min at 20 °C, and the stamps were dried under a nitrogen flow. A solution was then prepared by mixing 40 µl human FN (Merck) and 960 µl of demineralized water. A volume of 100 µl of this solution was deposited on top of each stamp for 1 h at room temperature in the dark. After gently removing the solution, a PDMS stamp was dried under a nitrogen flow and placed carefully in the centre of a PDMS-coated glass coverslip for 15 s. The PDMS stamps were then gently removed with tweezers and a pluronic solution at 5 mg ml^{-1} was incubated for 5 min at room temperature to passivate unprinted areas. These microprinted PDMS-coated glass coverslips were rinsed three times with sterile phosphate-buffered saline (PBS) and dried a under nitrogen flow.

Cell culture

Fish epithelial keratocytes were obtained from the scales of a Central American cichlid (*Hypsophrys nicaraguensis*)[29,46]. Scales were gently taken off the fish and placed in the centre of a microprinted PDMS-coated glass coverslip and covered with a drop of 150 µl of culture medium. The culture medium was composed of Leibovitz's L-15 medium (Thermo Fisher Scientific) supplemented with 10% fetal bovine serum (Capricorn), 1% penicillin/streptomycin (Westburg), 14.2 mM of 4-(2-hydroxyethyl)-1-piperazineethanesulfonic acid (HEPES; Sigma Aldrich) and 30% deionized water, which was placed on top of the scale. A glass coverslip 22 mm in diameter was deposited on top of the scales and a few drops of culture medium were added around the samples. Epithelial keratocytes were cultured in the dark at room temperature for 12 h.

Epithelial cells from the MDCK cell line (MDCK II, Sigma 85011435) were maintained in polystyrene T75 flasks in a cell culture incubator at 37 °C and 5% CO_2. MDCK cells were cultured in a proliferation medium composed of Dulbecco's modified Eagle's medium, high glucose (4.5 g l^{-1}) with L-glutamine (BE12-604F, Lonza) supplemented with 10% (v/v) fetal bovine serum (AE Scientific) and 1% penicillin and streptomycin antibiotics (AE Scientific).

Time-lapse imaging

Time-lapse microscopy experiments were carried out on a Ti-U inverted microscope (Nikon) equipped with a manual stage[29,46]. Differential interference contrast (DIC) images were taken every 3 min using a ×10, ×20 or ×40 objective and captured with a DS-Qi2 camera (Nikon) controlled with the NIS-Elements Advanced Research 4.0 software (Nikon). The cell clusters were tracked with the Manual Tracking plugin of FIJI.

Drug treatment

EGTA (Sigma Aldrich) was added to the normal medium at a final concentration of 2 mM to partially chelate the calcium in the medium.

Mitochondrial membrane potential

The mitochondrial membrane potential was measured using MT red, which stained active mitochondria in live cells by binding thiol-reactive chloromethyl groups in the mitochondrial membrane. A concentration of 50 nM of the MT red dye (Invitrogen) was used for 30 min at room temperature to allow dye equilibration across the plasma and inner mitochondrial membranes. For imaging, the medium containing the MT red dye was replaced with fresh normal medium.

Immunofluorescence and confocal microscopy

Fish keratocytes were fixed and permeabilized with 4% paraformaldehyde and 0.2% Triton X-100 in PBS for 15 min at room temperature. The samples were then incubated with 1% bovine serum albumin (BSA) in PBS for 30 min at room temperature, followed by sequential incubation with primary and secondary antibodies diluted with 1% BSA in PBS for 45 min at 37 °C. Actin filaments were stained with Alexa Fluor 488 phalloidin (Invitrogen, 1:200), the nucleus with 4′,6-diamidino-2-phenylindole (DAPI; Invitrogen, 1:200), microtubules with an anti-tubulin antibody produced in mouse (1:200) and the Golgi apparatus with 10 µg ml^{-1} wheat germ agglutinin conjugated with Alexa Fluor 594. Images were collected in epifluorescence and confocal mode with a motorized inverted microscope (A1R HD25, Nikon) equipped with ×20, ×40 and ×60 objectives (numerical aperture 1.45, oil immersion; Plan Apo) and ×100 silicone objectives (Plan Apo) and lasers that span the violet (405 and 440 nm), blue (457, 477 and 488 nm), green (514 and 543 nm), yellow-orange (568 and 594 nm) and red (633 and 647 nm) spectral regions. Epifluorescence images were recorded with a photometrics camera (Prime 95B, Photometrics) using the NIS-Elements Advanced Research 4.5 software (Nikon). Confocal images were recorded with ×100 Plan Apo silicone objective of high numerical aperture (Plan Apochromat Lambda S ×100 Silicone, Nikon) in galvanometric mode with small *Z*-depth increments (0.1 µm) and a pinhole of 12 µm to capture high-resolution images. Confocal images were processed using NIS-Elements (Nikon, Advanced Research v.4.5).

Polyacrylamide hydrogels

Polyacrylamide gel substrates of 18 kPa were prepared as previously described[48]. Briefly, glass-bottomed dishes (35 mm; MatTek) were treated with a solution of 714 µl of acetic acid (%) and 714 µl of silane in 10 ml of ethanol (96%) for 20 min. After the removal of the solution, the dishes were rinsed twice with ethanol (96%) and dried under a nitrogen flow. For 18 kPa gels, a solution of 0.65 mg of *N*-hydroxyethyl acrylamide in 5 ml of PBS was prepared. Then, 820 µl of this solution was mixed in a microcentrifuge tube (1.5 ml; Eppendorf) with 100 µl bisacrylamide (2%), 80 µl acrylamide (40 %) and 3 µl red fluorescent carboxylate-modified beads (0.2 µm; red 580/605, Life Technologies). The samples were degassed under vacuum for at least 20 min. Then 0.5 µl of *N*,*N*,*N*′,*N*′-tetramethyl ethylenediamine (TEMED) with 5 µl of ammonium persulfate was added to initiate the polymerization. 25 µl of the solution was carefully put on each glass-bottomed dishes and 18 mm glass coverslips (previously treated under corona) were placed on top of them. After 1 h of polymerization under an oxygen-free atmosphere, the coverslips were removed from the gels in hot water with tweezers. PDMS stamps were then used to create a micropattern in the FN on each gel. After washing the stamps in an ethanol solution (70%) for 15 min in an ultrasonic bath and drying under a nitrogen flow, a corona was applied for 30 s to make them more hydrophilic. A solution was prepared by mixing 70 µl human plasma FN (Merck), 20 µl green fibrinogen and 910 µl PBS. Then, 100 µl of this solution was put on top of each stamp for 1 h at room temperature in the dark.

After removing the solution, the stamps were dried under a nitrogen flow and deposited carefully into the centre of each gel. We carefully pressed on each corner of the stamp with tweezers to allow protein transfer. The printing process occurred overnight at 4 °C in the dark. Stamps were then gently removed with PBS, and gels were rinsed three times with PBS. BSA solution (5 mg ml^{-1}) was then used for 4 h at and 4 °C to passivate areas without any protein on the gels followed by three rinses with PBS. Cells were then seeded on microprinted hydrogels.

Traction force microscopy

Fluorescent beads 200 nm in diameter were homogeneously added to a polyacrylamide solution before polymerization. Their position was imaged over time with an IX83 inverted microscope equipped with a 632/22 excitation filter (incorporated in the Spectra-X light engine), a glass dichromatic mirror (Olympus) and an emission filter (FF01-692/40-25, Semrock). A reference image was obtained after the cells were removed by trypsinization. The two-dimensional displacement field was computed using a custom implementation of particle image velocimetry in Matlab (MathWorks). We used Fourier-transform traction microscopy[43,49] and filtered the displacement field with a predictor–corrector filter approach. The criteria for filtering were selected through semiquantitative approaches to ensure that the noise in cell-free areas was acceptable compared to the cell traction. Experimental and digital noise in the displacement field were minimized using a high density of fiducial markers, an appropriate size and overlap of the interrogation window for particle image velocimetry, and an algorithm to avoid peak-locking effects[43]. Noise in the measured displacement field was reduced by implementing a predictor–corrector filter approach, as described in ref. 50. We used a combination of filter power $z = 0.01$ and kernel size of 2.

Monolayer stress microscopy

We employed MSM[44] to quantify the spatial distribution of intracellular stress in cell clusters. This method is based on force equilibrium between cell–substrate traction and cell–cell stress. The first step in implementing MSM was to retrieve the local traction exerted by the monolayer on its substrate. We considered a cohesive monolayer composed of adjacent cells that created a uniform, flat, thin sheet. This indicates that its height was negligible in comparison to the lateral extent of the monolayer[44]. In that case, stress within the monolayer and the underlying traction exerted by the monolayer upon its substrate were taken to be planar with no out-of-plane contributions. The stress everywhere in a monolayer was then determined by terms arising from traction and boundary conditions. Given that a monolayer consistently maintained its mechanical equilibrium, Newton's laws dictate that this balance of forces must be unaffected by the material properties of the monolayer[44]. MSM was implemented, as custom-made software, in Python v.3 using different libraries (NumPy, SciPy, Matplotlib, scikit-image, pandas, pyFFTW, opencv and cython).

Statistical analysis

Each experiment was repeated at least three times. Each set of data was tested for normality using the d'Agostino–Pearson test in Prism 10.0 (GraphPad), which combines tests for skewness and kurtosis to determine whether the shape of the data distribution was similar to the shape of a normal distribution. For paired comparisons, significances were calculated in Prism 10.0 (GraphPad) with a Student's *t*-test (two-tailed, unequal variances) when the distributions proved to be normal. If a dataset did not pass the normality tests, the significances were calculated with Mann–Whitney (two-tailed, unequal variances). For multiple comparisons with a non-normal distribution, datasets were analysed with a Kruskal–Wallis test in Prism 10.0 (GraphPad), which is a suitable nonparametric test for comparing several independent groups when data are skewed. When the null hypothesis was not retained ($P < 0.05$), Kruskal–Wallis was corrected with Dunn's test, which is a nonparametric test with no pairing and multiple comparisons and can be used for both equal and unequal sample sizes. Unless otherwise stated, all data are presented as mean ± standard deviation (s.d.). The confidence interval in all experiments was 95%. Details of the statistical parameters are included in all figure captions, namely $^{*}P < 0.05$, $^{**}P < 0.01$, $^{***}P < 0.001$ and $^{****}P < 0.0001$.

Ethical compliance

The use of primary epithelial cells, keratocytes, harvested from the scale of *Hypsophrys nicaraguensis* was done in accordance with European guidelines for animal experimentation and with the agreement of the local ethics committee of the University of Mons, which reviewed the procedure.

Data availability

All data are available from the corresponding authors upon request. Source data are provided with this paper.

Code availability

Codes are available at https://github.com/dbrueckner/CellTrains.

References

45. Hamieh, M. et al. Influence of substrate properties on the dewetting dynamics of viscoelastic polymer films. *J. Adhes.* **83**, 367–381 (2007).
46. Riaz, M., Versaevel, M., Mohammed, D., Glinel, K. & Gabriele, S. Persistence of fan-shaped keratocytes is a matrix-rigidity-dependent mechanism that requires $\alpha_5\beta_1$ integrin engagement. *Sci. Rep.* **6**, 34141 (2016).
47. Coppée, S., Gabriele, S., Jonas, A. M., Jestin, J. & Damman, P. Influence of chain interdiffusion between immiscible polymers on dewetting dynamics. *Soft Matter* **7**, 9951–9955 (2011).
48. Luciano, M. et al. Cell monolayers sense curvature by exploiting active mechanics and nuclear mechanoadaptation. *Nat. Phys.* **17**, 1382–1390 (2021).
49. Bruyère, C. et al. Actomyosin contractility scales with myoblast elongation and enhances differentiation through YAP nuclear export. *Sci. Rep.* **9**, 15565 (2019).
50. Schrijer, F. F. J. & Scarano, F. Effect of predictor–corrector filtering on the stability and spatial resolution of iterative PIV interrogation. *Exp. Fluids* **45**, 927–941 (2008).

Acknowledgements

M.L., E.V. and S.G. acknowledge funding from the European Regional Development Fund (ERDF) Prostem Research Project (No. 1510614, Wallonia DG06), the Epiforce Project of the National Fund for Scientific Research, Belgium (FRS-FNRS; Project No. T.0092.21), the Cellsqueezer Project of FRS-FNRS (Project No. J.0061.23), the Optopattern Project of FRS-FNRS (Project no. U.NO26.22) and the Interreg MAT(T)ISSE project, which is financially supported by Interreg France-Wallonie-Vlaanderen, ERDF). A.R. and M.L. are financially supported by FRS-FNRS as a research fellow (Aspirant FNRS) and Postdoctoral Researcher (Chargée de Recherches FNRS), respectively. E.V. and Y.K. are financially supported by FRS-FNRS through grants from the Fund for Research Training in Industry and Agriculture (FRIA). This project was supported by the European Research Council under the European Union's Horizon 2020 Research and Innovation Programme (Grant Agreement No. 851288 to E.H.) and Marie Skłodowska-Curie Actions (Grant Agreement No. 797621 to M.G.-G.). D.B.B. was supported by the NOMIS foundation as a NOMIS fellow and by the European Molecular Biology Organization (Postdoctoral Fellowship ALTF 343-2022) and performed this work in part at the Aspen Center for Physics, which is supported by the National Science Foundation (Grant No. PHY-1607611). X.T. and M.G.-G. acknowledge support from the Government of Catalonia (Grant No. AGAUR SGR-2017-01602 and a CERCA Programme), the

Spanish Ministry for Science and Innovation and ERDF (Grant No. PGC2018-099645-B-I00), the European Research Council (Grant No. Adv-883739), Fundació la Marató de TV3 (201903-30-31-32), the European Commission (Grant No. H2020-FETPROACT-01-2016-731957), La Caixa Foundation and the Biomedical Research Center Consortium in Red (Grant No. CB15/00153) at the Carlos III Health Institute, Ministry of Science and Innovation. IBEC is recipient of a Severo Ochoa Award of Excellence from the Spanish Ministry of Economy, Trade and Business.

Author contributions

S.G. and E.V. conceived the project, and S.G. supervised the project. E.V. developed the minimal epithelial models and performed the cell experiments, tracking and imaging with A.R. The theoretical model was developed by D.B.B. and E.H. D.B.B. implemented and performed the simulations. A.R., L.R., Y.K. and M.L. contributed to the experiments. E.V., D.B.B., A.R., M.G.-G., X.T., E.H. and S.G. analysed the data. The article was written by E.V., D.B.B., E.H. and S.G. It was read and corrected by all authors, who all contributed to the interpretation of the results.

Competing interests

The authors declare no competing interests.

Additional information

Extended data is available for this paper at https://doi.org/10.1038/s41567-024-02532-x.

Supplementary information The online version contains supplementary material available at https://doi.org/10.1038/s41567-024-02532-x.

Correspondence and requests for materials should be addressed to David B. Brückner, Edouard Hannezo or Sylvain Gabriele.

Peer review information *Nature Physics* thanks Chwee Teck Lim and the other, anonymous, reviewer(s) for their contribution to the peer review of this work.

https://doi.org/10.1038/s41567-024-02532-x

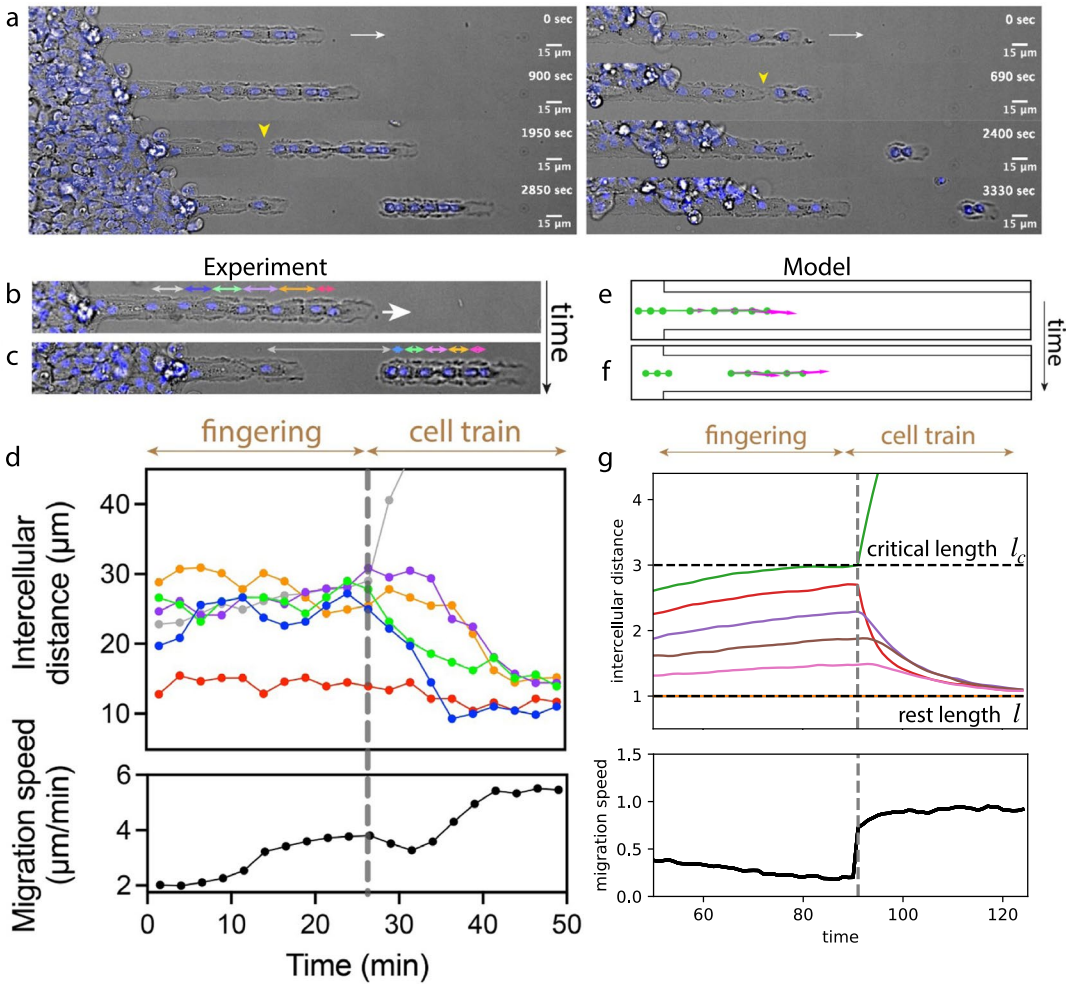

Extended Data Fig. 1 | Digitation of a primary epithelial tissue and fragmentation into cell trains. (a) Time-lapse sequences in Differential Interference Contrast (DIC) mode of the formation of cell trains of L = 6 cells (left) and L = 2 cells (right) from the fragmentation of monolayer extensions formed on 15 µm wide micropatterns. Nuclei are stained in blue with Hoechst 33342. White arrow shows the direction of migration and yellow arrows the fragmentation sites. Scale bars are 15 µm. **(b)** Time lapse sequence in DIC mode of the extension of a 'finger' of epithelial keratocytes on a 15 µm wide microstripe, which remained attached to the cell mass. Nuclei are stained in blue with Hoechst 33342. White arrow shows the direction of migration, while arrows in red, orange, purple, green and blue and yellow represent the intercellular distance (l) between five first individual cells within the tissue extension. The grey arrow corresponds to the intercellular distance at the fragmentation site. Intercellular distances are determined by the distance between nuclei. **(c)** At severe stretching, the tissue extension fragments into an autonomous cell train. Scale bars are 15 µm. **(d)** Evolution of intercellular distances versus time during the fingering process and after the fragmentation (grey dashed line). The intercellular distances are color-coded to their position from front to rear: red, orange, purple, green and blue. The grey dots represent the intercellular distance at the fragmentation site. The migration speed of the leading front is indicated in black. **(e-g)** Equivalent plots for simulations of the fingering process, which back cells simulated to be slowly moving. The initial fragmentation process allows to infer a critical length of the cell-cell contacts, which is estimated as $l_c \approx 3\,l$ (see Supplementary Theory Note for details).

https://doi.org/10.1038/s41567-024-02532-x

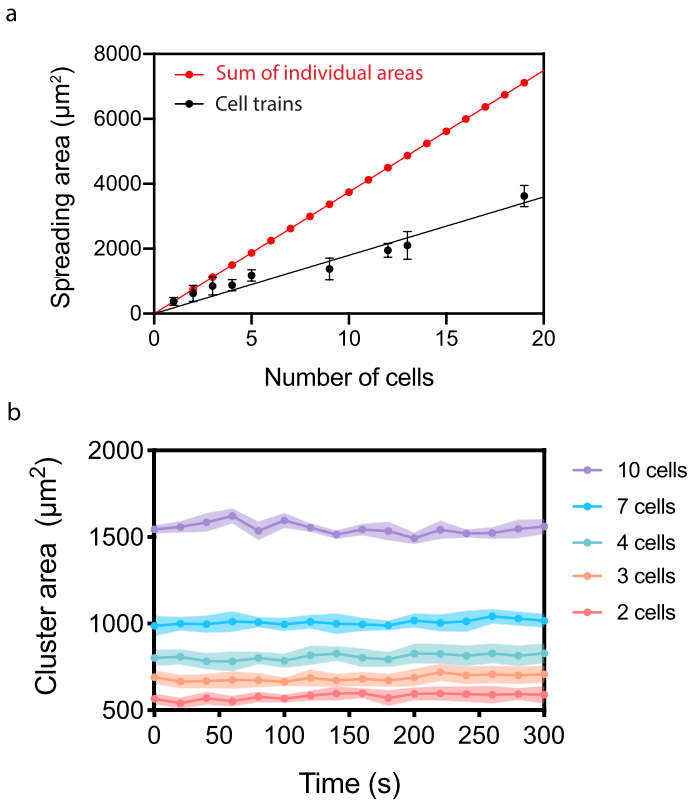

Extended Data Fig. 2 | Autonomous cell trains are compacted and cohesive units. (a) The cluster area is linearly correlated with the number of cells (black points) and smaller than the sum of individual cell areas (red points), suggesting that cells in one-dimensional epithelial clusters are significantly compacted. **(b)** The cluster area is constant over time, regardless the number of cells, demonstrating that one-dimensional epithelial clusters move as a single and cohesive unit. Error bars denote standard deviations. Data are Mean ± S.D.

https://doi.org/10.1038/s41567-024-02532-x

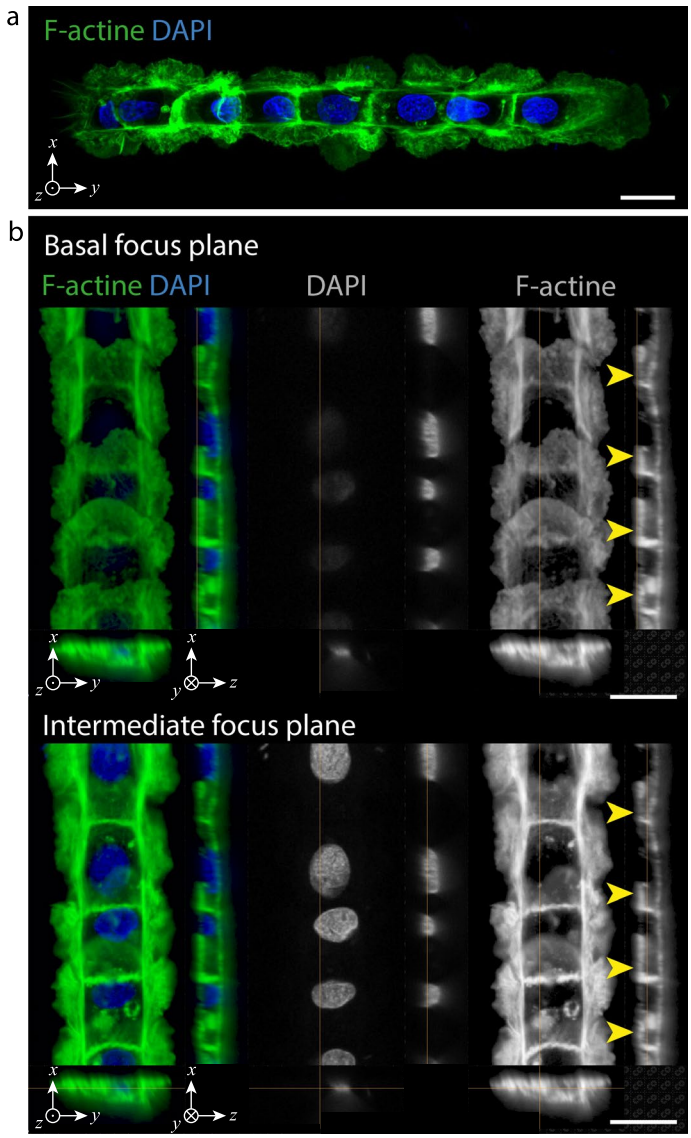

Extended Data Fig. 3 | Cell trains are composed of cryptic lamellipodia that invade underneath the adjoining cell. (a) Normal view in high resolution confocal mode of a cryptic lamellipodia in a cell train of 15 µm wide composed of 8 cells. **(b)** Zoomed side views of basal and intermediate focal planes indicating the presence of cryptic lamellipodia (yellow arrows) that extend underneath the cell body of the preceding cell. Actin is labelled in green with Phalloidin and DNA in blue with DAPI. The white arrows show the position of typical cryptical lamellipodia. Scale bars are 15 µm.

https://doi.org/10.1038/s41567-024-02532-x

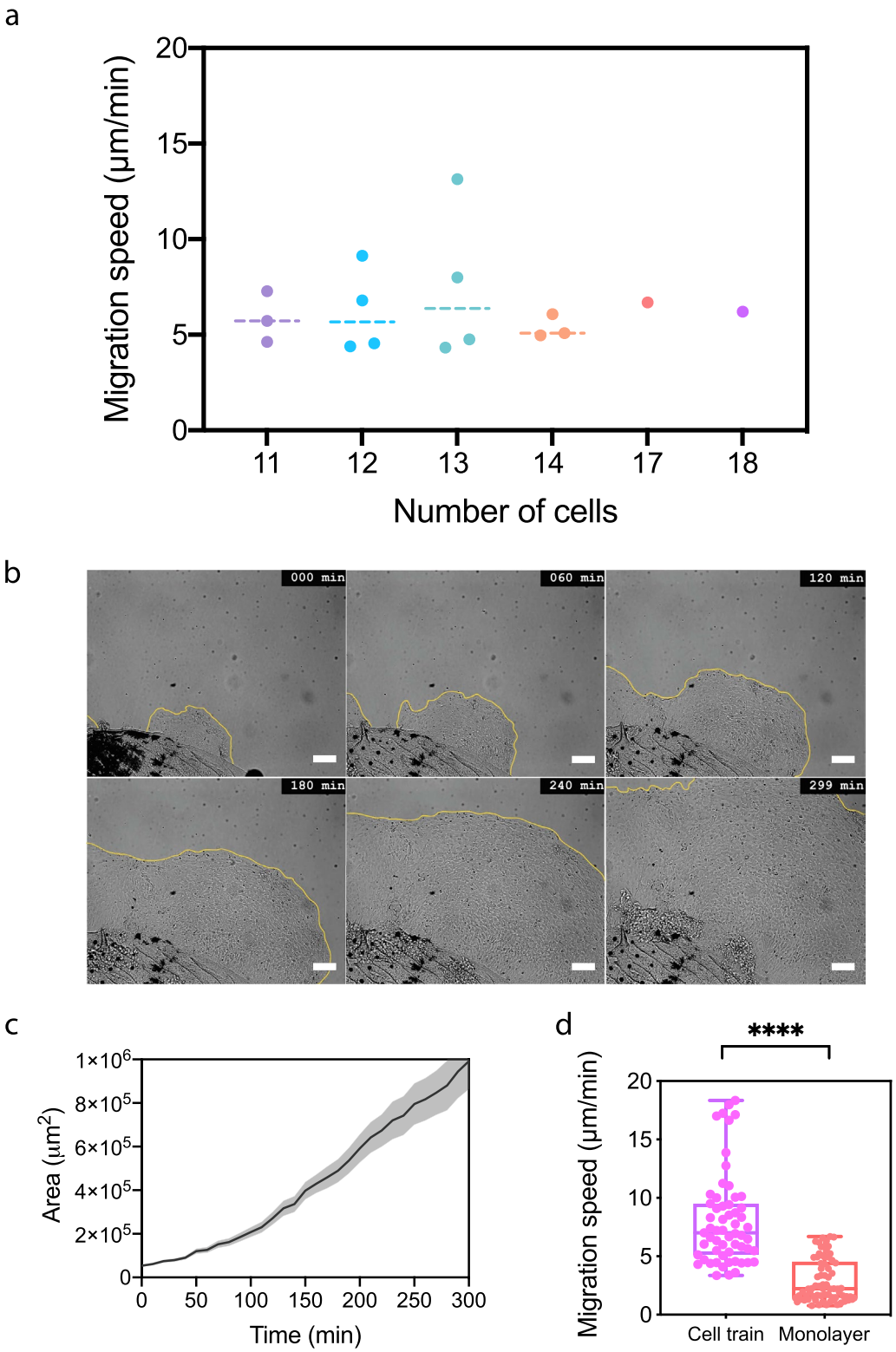

Extended Data Fig. 4 | Migration of very long autonomous cell trains and extension of a primary epithelial monolayers. (a) Migration speed of very long cell trains. Each point represents the mean migration speed of one cell train, whose length ranges from 11 to 18 cells. Dashed lines represent the median. The migration speed was calculated from time-lapse experiments of 45 min. The total number of cell trains is 16. **(b)** Representative time-lapse sequence in DIC mode of an epithelial monolayer of primary keratocytes growing out of a fish scale during 299 min. The growing front is depicted with a yellow line. The scale bar is 100 µm. (**c**) Evolution of the monolayer area over time (n = 3, mean ± S.D.). (**d**) Migration speed for one-dimensional clusters ('cell train' in pink, n = 62) and epithelial monolayers ('monolayer' in light red, n = 74) with ****$p < 0.0001$.

https://doi.org/10.1038/s41567-024-02532-x

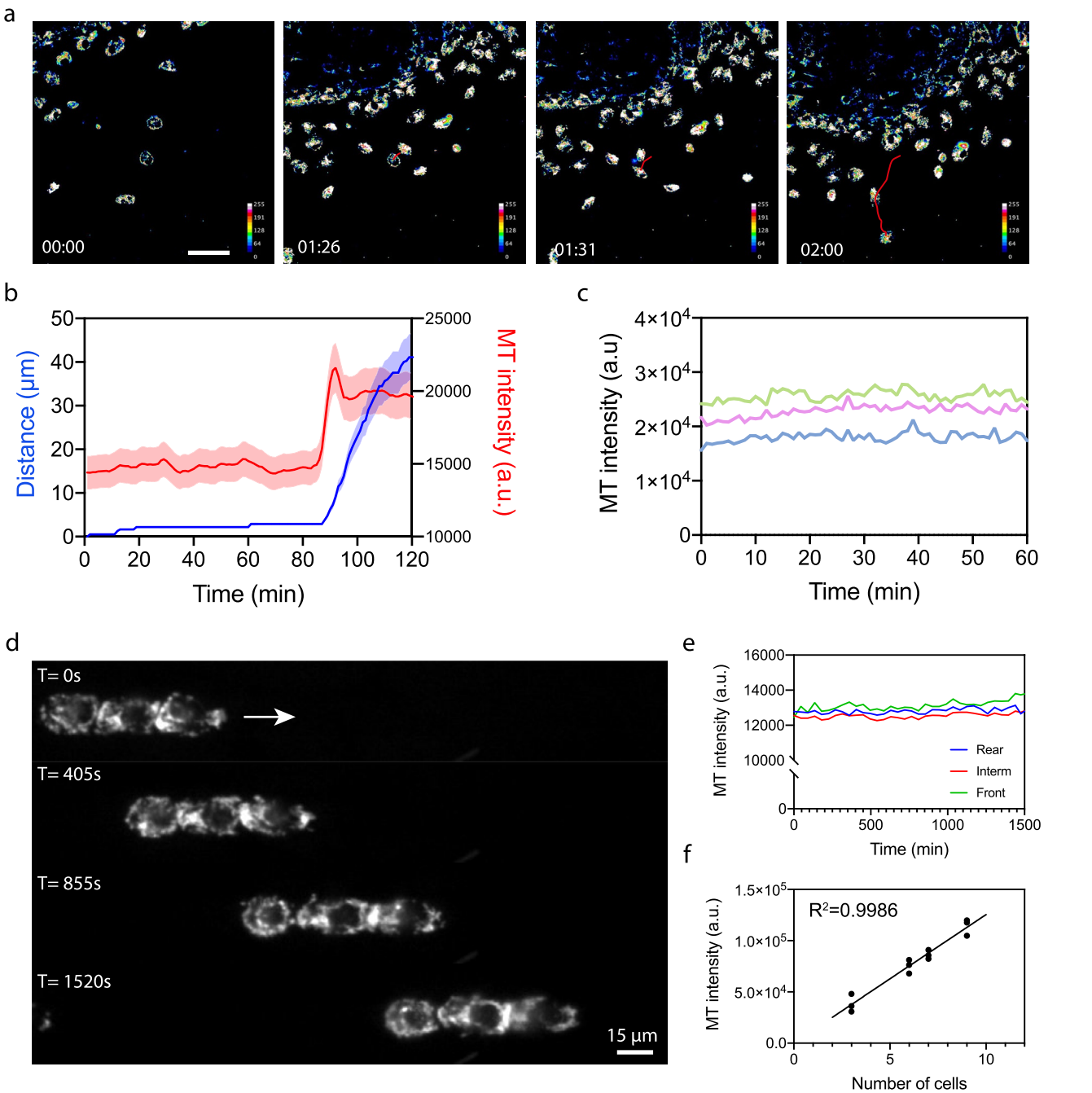

Extended Data Fig. 5 | The mitochondrial membrane potential increases as the cell polarizes and remains constant during migration. (a) Typical time-lapse sequence in epifluorescence mode of single epithelial cells stained with red MitoTracker (MT) that stained active mitochondrial in live cells by binding thiol-reactive chloromethyl groups in the mitochondrial membrane. Cells were digitized in 256 bits and the MitoTracker intensity was color-coded (from high to low: white, purple, red, orange, yellow, green, light blue and dark blue). The redline shows the displacement of a cell that started to polarize and migrate at 86 min. The scale bar is 30 µm. **(b)** Evolution of the distance (in blue) and the MT intensity (in red) over time (n = 3, mean ± S.D.) **(c)** Evolution of the MT intensity of three individual polarized cells that migrate during 60 min. **(d)** Typical time-lapse sequence of a cell train (L = 3 cells) migrating on a fibronectin microstripe of 15 µm wide and labeled in live conditions with mitotracker red. The total duration is 1520 sec. and the scale bar is 15 µm. **(e)** Temporal evolution of the mitochondrial potential membrane intensity per cell in cell trains of L = 3 cells (n = 6 cell trains). **(f)** Linear evolution of the mitotracker intensity for cell trains of L = 3, 6, 7 and 9 cells (n = 3 for each condition) with $R^2 = 0.9986$.

https://doi.org/10.1038/s41567-024-02532-x

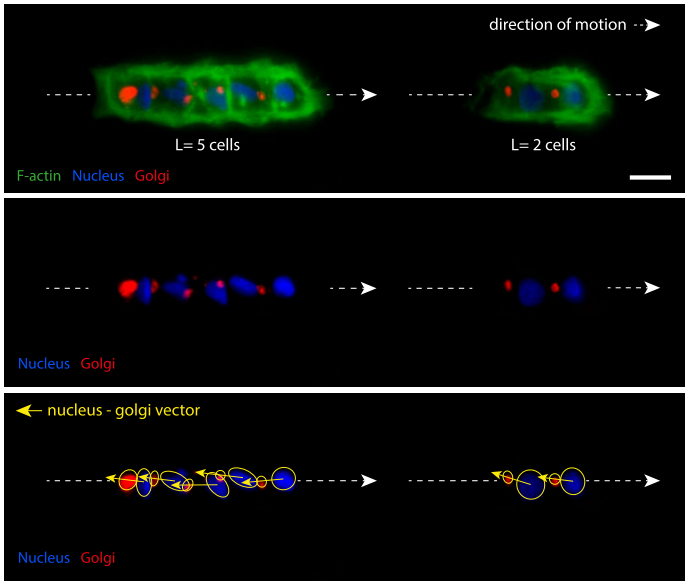

Extended Data Fig. 6 | The Golgi complex is positioned behind the nucleus in cell trains. Epifluorescent images of trains of cells composed of L = 5 (left) and L = 2 (right) cells migrating on fibronectin microstripes of 15 µm wide. Keratocytes were labelled for the F-actin (green), the Golgi complex (red) and the nucleus (blue). The direction of motion is depicted by a white arrow and the orientation of the Golgi complex relative to the nucleus is indicated by a yellow arrow. The white dashed line represents the cell train axis. The scale bar is 15 µm.

https://doi.org/10.1038/s41567-024-02532-x

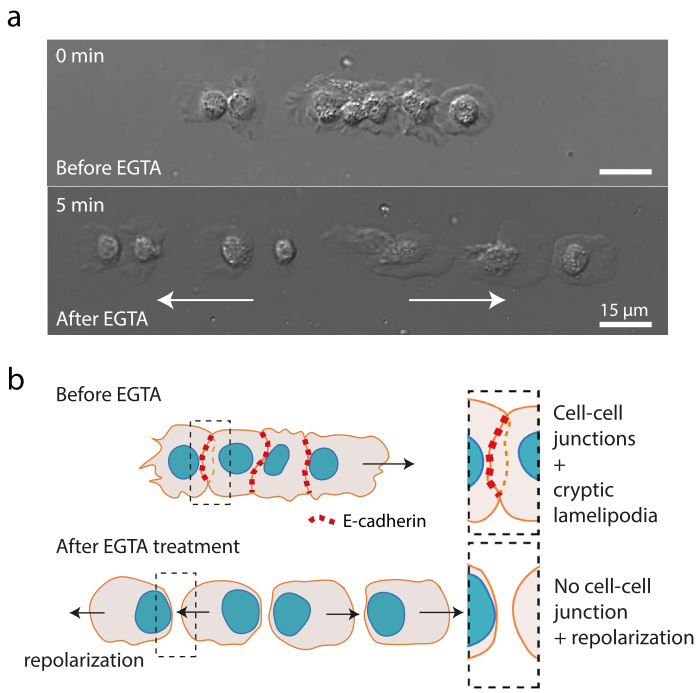

Extended Data Fig. 7 | Disruption of cell-cell adhesions with EGTA treatments leads to the increase of the migration speed and repolarization events. **(a)** Typical microscopy images in DIC mode of a one-dimensional epithelial cluster migrating on a 15 µm wide micropatterns before (t = 0 min) and after (t = 5 min) EGTA treatments. White arrows show the cell repolarization. Scale bars are 15 µm. **(b)** Schematic representation of the EGTA effect that disrupts adherens cell-cell adhesions due to a weakening of the rigid extracellular domain of E-cadherin and leads to repolarization events. **(c)** Migration speed of single cells on 15 µm wide microstripes (control: n = 57, EGTA: n = 32, in red), cell trains on 15 µm wide microstripes (control: n = 88, EGTA: n = 49, in purple), epithelial clusters on 30 µm wide microstripes (control: n = 51, EGTA: n = 57, in blue) and whole epithelial monolayers (control: n = 37, EGTA: n = 28, in grey). Data are Mean ± S.D. Control data are circles and EGTA-treated data are lozenges, ns is non-significant and ****$p < 0.0001$.

https://doi.org/10.1038/s41567-024-02532-x

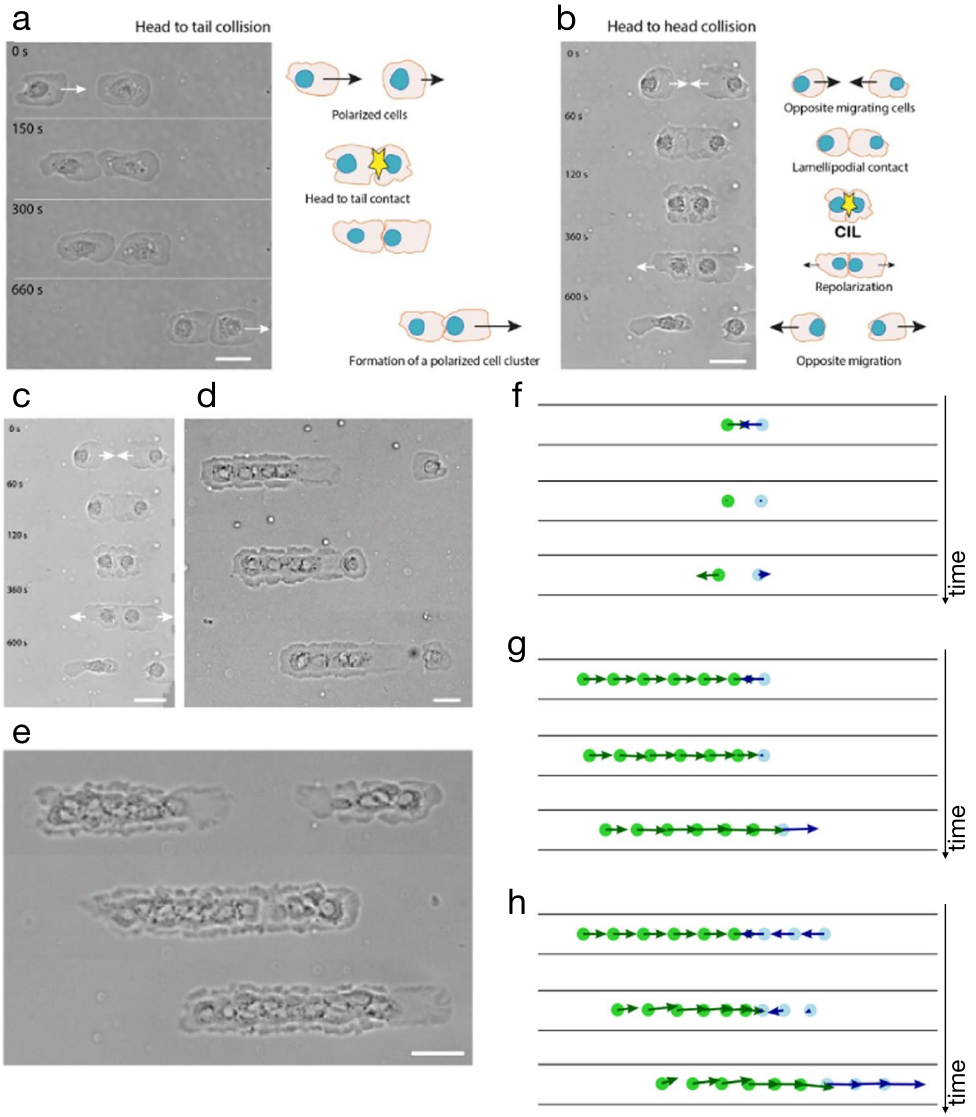

Extended Data Fig. 8 | Different collision scenarii between single epithelial cells and cell clusters. The collision configuration between two single epithelial cells induces an attractive or repulsive response. **(a)** Head-to-tail collisions promote the formation of a contact between a cell lamellipodia and the tail of a neighbouring cell, leading to the formation of a polarized cell doublet. (**b**) Head-to-head collisions between individual epithelial cells show a repulsive response of both cells that repolarized rapidly in opposite directions. Collisions events between **(c)** two opposite single cells, **(d)** a single cell against a cell train and **(e)** two cell trains always lead to the repolarization of the smaller cluster. Simulations of collision between **(f)** two opposite single cells, **(g)** on single cell against a cell train and **(h)** two cell trains show a repulsive response of both individual cells that repolarized rapidly in opposite directions and the repolarization of the shorter cluster, as observed experimentally in (c-e).

https://doi.org/10.1038/s41567-024-02532-x

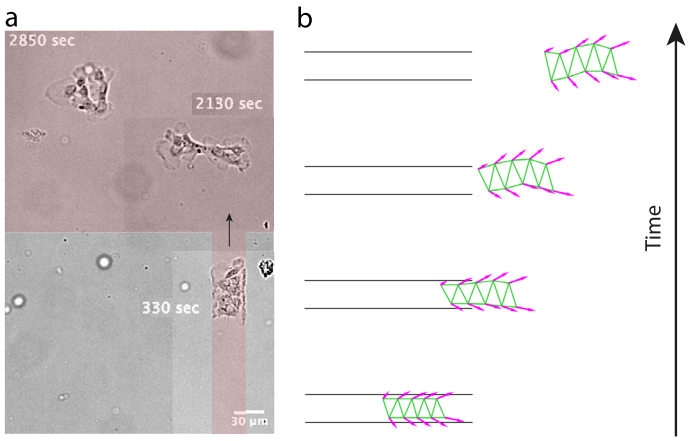

Extended Data Fig. 9 | Unconfined migration of a cell cluster. (a) Time-lapse sequence in differential Interference Contrast (DIC) mode of a cell cluster reaching the end of a 30 µm wide adhesive microstripe and entering a free open adhesive space. Upon exiting the microstripe, the cell cluster rapidly develops lamellipodia in the lateral directions away from their neighbours and finally breaks apart. The black arrow shows the direction of migration, while the light red zones indicate the microprinted adhesive areas. **(b)** Theoretical simulation of the unconfined migration of a one-dimensional epithelial cluster migrating out of a confined zone from the left to the right.

https://doi.org/10.1038/s41567-024-02532-x

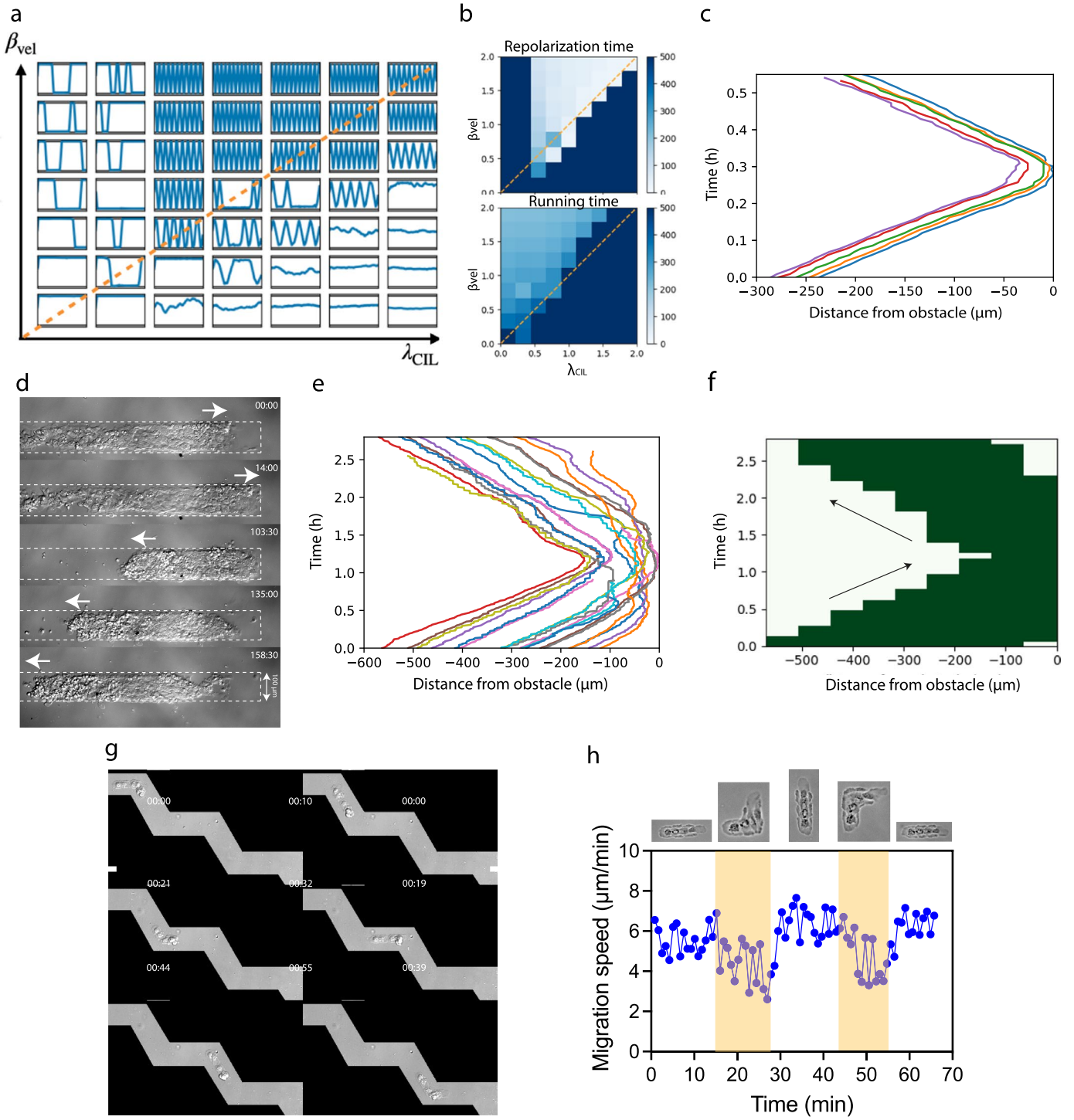

Extended Data Fig. 10 | Perturbation of the polarization of epithelial cell clusters by migrating against an obstacle and in complex turns. (a) Phase diagram showing trajectories of cell cluster center of mass in obstacles at both ends of the microstrip, as a function of the interaction parameters β_{vel} and λ_{CRL}. **(b)** Phase diagrams of repolarization and running times as a function of β_{vel} and λ_{CRL}, quantifying the repolarization and running phases in panel (b). **(c)** Distance travelled over time by individual cells within the cell train moving towards the border of a 15 μm-wide fibronectin microstripe (from left to right) during 51 min. After reaching the micropattern extremity on the left part, the cell train compacted against the border, then epithelial cells repolarized, and the cluster migrated in the opposite direction (from right to left). Each color-coded line corresponds to one cell. **(d)** Time-lapse sequence of the migration of a 100 μm wide epithelial cluster moving towards the border of a fibronectin microstripe (left to the right) during 158 min. After reaching the micropattern extremity on the left part, the wide cluster compacted against the border, then epithelial cells repolarized and the whole cluster migrated in the opposite direction (right to left). **(e)** Distance travelled over time by individual cells within the 100 μm wide cluster presented in (d). Each color-coded line corresponds to the one cell. **(f)** Kymograph of the spatial position over time of the 100 μm wide cluster presented in (d), showing its repolarization after the collision. The slopes before and after the collision indicated similar migrating velocities. **(g)** Time-lapse sequence in DIC mode of a cell train migrating on a microstripe of 15 μm wide with corners of 120°. The total duration time is 55 min and scale bars are 15 μm. **(h)** Representative example of the decrease of the instantaneous velocity of a cell train (L = 4 cells) around corners of 90°.